pubs.acs.org/Biomac

Article

Near-Infrared Fluorescent Micelles from Poly(norbornene) Brush Triblock Copolymers for Nanotheranostics

Carolyne B. Braga, Ronaldo A. Pilli,* Catia Ornelas,* and Marcus Weck*

Cite This: *Biomacromolecules* 2021, 22, 5290−5306

Read Online

ACCESS | Metrics & More | Article Recommendations | Supporting Information

ABSTRACT: This contribution describes the design and synthesis of multifunctional micelles based on amphiphilic brush block copolymers (BBCPs) for imaging and selective drug delivery of natural anticancer compounds. Well-defined BBCPs were synthesized via one-pot multi-step sequential grafting-through ring-opening metathesis polymerization (ROMP) of norbornene-based macroinitiators. The norbornenes employed contain a poly(ethylene glycol) methyl ether chain, an alkyl bromide chain, and/or a near-infrared (NIR) fluorescent cyanine dye. After block copolymerization, post-polymerization transformations using bromide−azide substitution, followed by the strain-promoted azide−alkyne cycloaddition (SPAAC) allowed for the functionalization of the BBCPs with the piplartine (PPT) moiety, a natural product with well-documented cytotoxicity against cancer cell lines, via an ester linker between the drug and the polymer side chain. The amphiphilic BBCPs self-assembled in aqueous media into nano-sized spherical micelles with neutral surface charges, as confirmed by dynamic light scattering analysis and transmission electron microscopy. During self-assembly, paclitaxel (PTX) could be effectively encapsulated into the hydrophobic core to form stable PTX-loaded micelles with high loading capacities and encapsulation efficiencies. The NIR fluorescent dye-containing micelles exhibited remarkable photophysical properties, excellent colloidal stability under physiological conditions, and a pH-induced disassembly under slightly acidic conditions, allowing for the release of the drug in a controlled manner. The *in vitro* studies demonstrated that the micelles without the drug (blank micelles) are biocompatible at concentrations of up to 1 mg mL^{-1} and present a high cellular internalization capacity toward MCF-7 cancer cells. The drug-functionalized micelles showed *in vitro* cytotoxicity comparable to free PPT and PTX against MCF-7 and PC3 cancer cells, confirming efficient drug release into the tumor environment upon cellular internalization. Furthermore, the drug-functionalized micelles exhibited higher selectivity than the pristine drugs and preferential cellular uptake in human cancer cell lines (MCF-7 and PC3) when compared to the normal breast cell line (MCF10A). This study provides an efficient strategy for the development of versatile polymeric nanosystems for drug delivery and image-guided diagnostics. Notably, the easy functionalization of BBCP side chains via SPAAC opens up the possibility for the preparation of a library of multifunctional systems containing other drugs or functionalities, such as target groups for recognition.

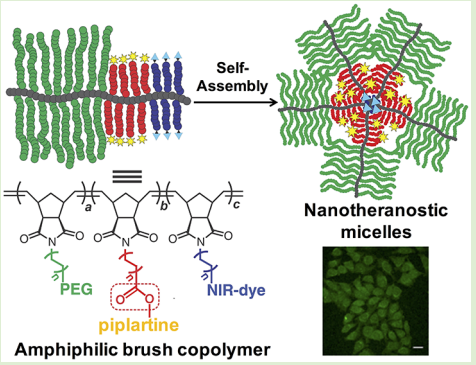

INTRODUCTION

Chemotherapy is currently the most widely adopted strategy for treating various types of cancer, playing a fundamental role both in cure and in extension of patients' survival.[1,2] Owing to the lack of targeting capability and non-specific accumulation, however, chemotherapeutic agents attack non-cancer cells, leading to acute side effects. In addition, since most anticancer compounds have low water solubility and consequently limited bioavailability, they require to be solubilized using high concentrations of surfactants or co-solvents, frequently leading to adverse effects.[3,4] These limitations compromise the success of treatments, and recent research efforts have focused on developing new and more precise delivery strategies.

Research in cancer nanomedicine has achieved significant progress in recent years through the development of nanocarriers that improve the biodistribution, effectiveness, tumor targeting, and accumulation, thereby enabling the enhancement of the balance between the therapeutic efficacy, selectivity, and overall toxicity of chemotherapeutic drugs.[5−9] Since the successful development of Doxil (PEGylated liposomes containing doxorubicin) as the first FDA-approved nanodrug,[10] a range of nanomedicines have received regulatory approval or are under clinical investigation for the treatment of various types of cancer.[11−13] Nanomaterial-based drug delivery systems have shown prominent accumulation in tumors mediated by the enhanced permeability and retention (EPR)

Received: September 12, 2021
Revised: October 21, 2021
Published: November 15, 2021

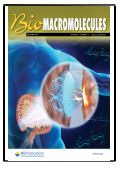

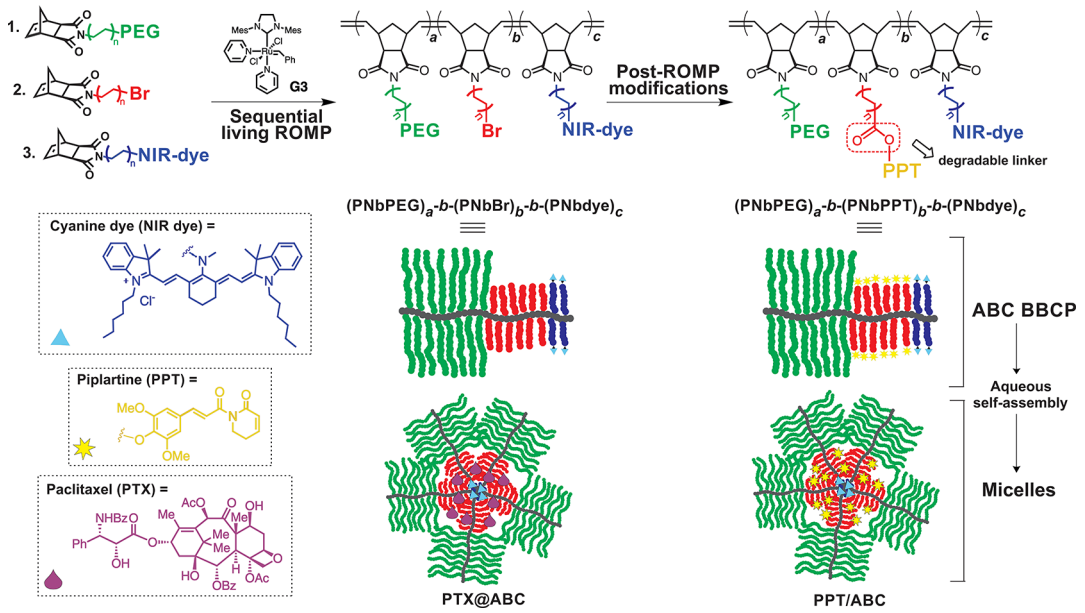

Figure 1. Schematic illustration of the synthesis of well-defined amphiphilic brush block copolymers (BBCPs) and the preparation of multifunctional fluorescent polymeric micelles from BBCPs.

effect, which is based on the high permeability of the tumor vasculature to nanomedicines due to disordered endothelial cells and large fenestrations, in addition to the poorly lymphatic drainage in tumor tissues that causes the retention of the nanomaterials.[5,7,9] To exploit the EPR-based tumor targeting following systemic delivery, physicochemical properties of nanocarriers such as the size, surface charge, and shape have to be controlled to allow for selective extravasation into tumors based on anatomical differences between normal and diseased tissues to avoid unspecific interactions with blood components, to extend their circulation half-life and to prevent fast clearance.[14,15] Typical nanocarrier systems that address these issues include liposomes, vesosomes, dendrimers, polymeric nanoparticles, interlocked nanomaterials, and polymeric micelles.[16−23]

Polymeric micelles self-assembled from amphiphilic block copolymers represent a promising platform for drug delivery applications since their size is on the nanoscale (∼10−200 nm), therefore, effectively and selectively penetrating tumor tissues. Polymeric micelles are fabricated rapidly from a large library of inexpensive starting materials and have tunable solubilization/dispersion properties to engineer in vivo performance.[24−26] The properties of such micellar assemblies are strongly dependent on the architecture of their corresponding polymeric building blocks and, ultimately, the method employed in their synthesis. A variety of amphiphilic block copolymers with unique architectures have been investigated for drug delivery applications, including linear block copolymers and complex architectures such as brush and star-like polymers.[27−30]

Living ring-opening metathesis polymerization (ROMP) is one of the most powerful methods for synthesizing well-defined amphiphilic block polymers with controlled molecular weights (MW) and low dispersities ($Đ$).[31,32] The sequential ROMP of norbornene-based monomers following the "grafting-through" strategy is an effective methodology for the preparation of highly branched amphiphilic brush copolymers (also known as molecular brushes or bottlebrush copolymers) with unique self-assembly, drug delivery, and imaging capabilities.[29,32−38] This is possible due to the exceptional functional group tolerance of highly active Grubbs initiators and the mild reaction conditions required.[39]

A few reports have explored amphiphilic brush diblock and ABA-triblock copolymers synthesized via sequential ROMP for both drug delivery and imaging applications.[40−44] Amphiphilic poly(norbornene) diblock brush copolymers bearing a cholesterol block and a poly(ethylene glycol) (PEG) block were studied by Lu and co-workers for the delivery of the anticancer drug doxorubicin.[42] Cheng et al. reported poly(norbornene) diblock brush co-polymer−paclitaxel conjugates with acid-sensitive cyclic acetal-based linkages, which exhibited a sustained delivery of paclitaxel (PTX) into cancer cells.[43] Random ABC brush copolymers prepared through statistical ROMP have also been reported.[45] Despite these advances, the preparation of well-defined amphiphilic poly(norbornene) brush triblock copolymers via sequential ROMP for drug delivery applications is very limited.[46−48] Diblock and ABC-triblock copolymers with well-defined architectures designed to self-assemble into stimuli-responsive and near-infrared (NIR) fluorescent micelles that carry anti-cancer drugs, as the prepared ones in this work, introduces a new class of materials for nanotheranostics. Moreover, varying the composition and molecular weight will offer important insights into the structure-dependent properties and poly(norbornene) copolymers *in vitro*.

Natural products are an invaluable source of therapeutic agents and have driven drug discovery due to their broad spectrum of biological activity and specific molecular target.[49] Piplartine (PPT, also known as piperlongumine, Figure 1) is a naturally occurring alkaloid isolated from *Piper longum* L. (long pepper) that possesses multiple pharmacological activities such as anti-inflammatory, anxiolytic, antidepressant, antileishmanial, neuroprotective, antiplatelet, and antineoplastic activities.[50−52] PPT has been studied as a potential anticancer agent since it exhibits cytotoxicity against different types of cancer cells[50,51,53−58] and presents antitumor properties in animal models.[57,59,60] PPT induces cell death preferentially by elevating reactive oxygen species (ROS) levels in the

https://doi.org/10.1021/acs.biomac.1c01196
Biomacromolecules 2021, 22, 5290−5306

Table 1. Characterization Data of Amphiphilic BBCPs Synthesized by ROMP

BBCP code	type	experimental composition[a] [target composition[b]]	solvent	M_n (kDa) Theor.[a]	M_n (kDa) GPC[c]	M_n (kDa) NMR[d]	$Đ$[c,e]
1	AB	$(\mathbf{PNbPEG})_{30}$-*b*-$(\mathbf{PNbBr})_{59}$[c] [$(PNbPEG)_{30}$-*b*-$(PNbBr)_{70}$]	DCM	95.0	90.9	N.D.[f]	1.45
2	AB	$(\mathbf{PNbPEG})_{42}$-*b*-$(\mathbf{PNbBr})_{45}$[c] [$(PNbPEG)_{50}$-*b*-$(PNbBr)_{50}$]	DCM	132.9	112.7	N.D.	1.56
3	BA	$(\mathbf{PNbBr})_{40}$-*b*-$(\mathbf{PNbPEG})_{63}$[c] [$(PNbBr)_{30}$-*b*-$(PNbPEG)_{70}$]	DCM	170.7	159.4	N.D.	1.96
4	BA	$(\mathbf{PNbBr})_{68}$-*b*-$(\mathbf{PNbPEG})_{52}$[c] [$(PNbBr)_{50}$-*b*-$(PNbPEG)_{50}$]	DCM	132.9	143.5	N.D.	1.50
5	BA	$(\mathbf{PNbBr})_{77}$-*b*-$(\mathbf{PNbPEG})_{30}$[c] [$(PNbBr)_{70}$-*b*-$(PNbPEG)_{30}$]	DCM	95.0	97.4	N.D.	1.48
6	AB	$(\mathbf{PNbPEG})_{33}$-*b*-$(\mathbf{PNbBr})_{76}$[c] [$(PNbPEG)_{30}$-*b*-$(PNbBr)_{70}$]	DCE	95.0	104.3	N.D.	1.42
7	AB	$(\mathbf{PNbPEG})_{50}$-*b*-$(\mathbf{PNbBr})_{48}$[c,d] [$(PNbPEG)_{50}$-*b*-$(PNbBr)_{50}$]	DCE	132.9	132.3	131.7	1.46
8	AB	$(\mathbf{PNbPEG})_{70}$-*b*-$(\mathbf{PNbBr})_{29}$[c] [$(PNbPEG)_{70}$-*b*-$(PNbBr)_{30}$]	DCE	170.7	170.8	N.D.	1.64
9	ABC	$(\mathbf{PNbPEG})_{50}$-*b*-$(\mathbf{PNbBr})_{40}$-*b*-$(\mathbf{PNbdye})_{12}$[c,d] [$(PNbPEG)_{50}$-*b*-$(PNbBr)_{35}$-*b*-$(PNbdye)_{15}$]	DCE	141.0	110.7	140.1	1.70
10	BAC	$(\mathbf{PNbBr})_{17}$-*b*-$(\mathbf{PNbPEG})_{45}$-*b*-$(\mathbf{PNbdye})_{15}$[c,d] [$(PNbBr)_{35}$-*b*-$(PNbPEG)_{50}$-*b*-$(PNbdye)_{15}$]	DCE	141.0	92.4	122.9	1.90

[a]Experimental composition is used to identify polymers throughout the text. [b]Theoretical values were calculated from the initial monomer-to-**G3** molar ratio assuming [**G3**] = 1 equiv. and complete monomer conversion. Target number-average degree of polymerization (DP_n) values are subscripted after each block. [c]Determined via GPC calibrated with poly(styrene) standards (room temperature, 0.03 M LiCl in DMF, 1 mL min^{-1}). [d]M_n of the BBCP was estimated by first assuming complete conversion of **Nb-PEG** (**M1**) (as observed by GPC and ^{1}H NMR spectroscopy after polymerization of **M1**) and then comparing the integrations of selected ^{1}H NMR resonances of the hydrophobic segments to those of PEG at δ 3.60−3.40 ppm ($-CH_2CH_2-$) (see the Supporting Information for integrated spectra). [e]$Đ$ is the dispersity. [f]N.D. = not determined.

intracellular medium.[55,61,62] Additionally, ROS-independent mechanisms, such as caspase- and Bax-dependent apoptosis and/or necrosis, have also been reported to be associated with PPT's anticancer activity.[53,61] Studies on the structure−activity relationship (SAR) have indicated that the α,β-unsaturated δ-lactam moiety, acting as a Michael acceptor for nucleophiles available in the biological environment, is the key pharmacophore essential to its cytotoxicity and ROS-generating activity, whereas the exocyclic olefin is important for its potency.[63] This potential anticancer characteristic of PPT makes it an appealing compound for further development. One shortcoming of PPT, however, is its poor water solubility (26 μg/mL)[64] that affects its bioavailability and toxicity toward normal cells. Hence, the association of PPT to polymeric micelles offers great possibilities to overcome this drawback. Furthermore, a formulation of PPT in a suitable drug delivery system enables us to protect the lactam moiety from undesired chemical transformations in the biological medium before reaching its target.

Herein, we report a micellar nanoplatform based on amphiphilic BBCPs bearing both therapeutic and imaging functionality into a single system for nanotheranostics (Figure 1). The polymerization behavior of all new norbornenes, including their living character throughout the polymerization, was evaluated, and the ROMP conditions were optimized to tune the ratios of hydrophilic to hydrophobic chains. The well-defined AB-diblock and ABC-triblock BBCPs were synthesized through a one-pot multi-step sequential grafting-through ROMP initiated by a Grubbs' third-generation initiator. The diblock BBCPs are composed of a hydrophilic block with poly(ethylene)glycol (PEG) pendent side chains and a hydrophobic block containing alkyl bromide pendent side chains designed for posterior drug functionalization. The synthesized triblock BBCP features a third polymer block containing NIR fluorescent cyanine dye moieties in its side chains. Drug functionalization was accomplished by converting the terminal bromide groups to azides followed by the copper-free strain-promoted azide−alkyne cycloaddition (SPAAC) attaching a PPT derivative to the polymeric nanocarrier via an ester linker designed to undergo enzymatic hydrolysis in the tumor microenvironment. The BBCPs were characterized by ^{1}H NMR spectroscopy, Fourier transform infrared (FT-IR) spectroscopy, and gel-permeation chromatography (GPC). The self-assembly of these BBCPs was investigated by dynamic light scattering (DLS) and transmission electron microscopy (TEM). In addition, we also investigated the potential of these micellar assemblies to encapsulate the anticancer drug PTX. The photophysical properties of the NIR fluorescent micelles in aqueous solution, as well as the micellar stability and drug release profiles from the nanosystems at different pH conditions were evaluated. The *in vitro* cytotoxicity and cellular uptake of the micelles were explored against a panel of different cancer and normal cell lines.

EXPERIMENTAL SECTION

Materials and Methods. All reagents were purchased from commercial suppliers and used as received unless otherwise specified. All solvents were purchased with "certified ACS" grade or higher quality. Anhydrous solvents were either prepared with a solvent purification system by filtration of HPLC grade solvents through alumina or purchased in sealed bottles and used under an inert atmosphere. Column chromatography was performed using silica gel 60 Å (230−400 mesh) from Sorbent Technologies. Dialysis was performed using a Spectra/Por 6 dialysis membrane with a molecular weight cutoff (MWCO) of 8000 kDa after ROMP and 3500 kDa after azide−halide exchange and SPAAC reactions. RPMI-1640, Dulbecco's modified phosphate-buffered saline (DMPBS, pH 7.4), and 0.25% trypsin−EDTA solution (Gibco) were purchased from ThermoFisher Scientific (Itapevi, SP, Brazil). Fetal bovine serum (FBS) was purchased from Cultilab Materiais para Cultura de Células (Campinas, SP, Brazil). Cell Counting Kit-8 (CCK-8) was purchased from Sigma-Aldrich. Hoechst 33342 and Alexa Fluor 555 Phalloidin were obtained from Life Technologies. Instrumentation information can be found in the Supporting Information.

Synthesis of Norbornene-Based Monomers and Their Precursors. All monomers and their precursors used in this study were synthesized from *cis*-5-norbornene-*exo*-2,3-dicarboxylic anhydride (**1**). Detailed procedures for these syntheses are described in the Supporting Information.

Synthesis of the Clickable PPT Derivative and Its Precursors. Detailed procedures for these syntheses are described in the Supporting Information.

General Procedure for Sequential ROMP Polymerization. All bromo-functionalized brush (homo-, di-, or triblock) (co)-polymers were synthesized as follows. The brush triblock copolymer $(\mathbf{PNbPEG})_{50}$-*b*-$(\mathbf{PNbBr})_{40}$-*b*-$(\mathbf{PNbdye})_{12}$ is given as an example. First block: in a glovebox filled with N_2, the monomer **Nb-PEG** (**M1**)

https://doi.org/10.1021/acs.biomac.1c01196
Biomacromolecules 2021, 22, 5290−5306

(233.8 mg, 0.103 mmol, 50 equiv) was carefully added to the bottom of a small vial containing a stirring bar. Anhydrous and degassed 1,2-dichloroethane (DCE, 1755 μL) was added directly over the white solid via a micropipette, and the resulting solution (at a concentration of 0.059 M) was stirred gently to ensure complete dissolution of monomer **M1**. In another vial, a stock solution of Grubbs third-generation initiator (**G3**, 5 mg **G3** mL^{-1}, in DCE) was freshly prepared. The appropriate volume of solution of the **G3** initiator (300 μL, 2.06 × 10^{-6} mol, 1 equiv) was quickly added to the vial containing the monomer **M1** solution under stirring, achieving a final **M1** concentration of 0.05 M. The solution immediately turned from green to light brown, indicating the initiation of the polymerization. The viscous reaction mixture was capped and stirred at room temperature for 45 min until complete conversion of the first monomer. If only the brush homopolymer is desired, the polymerization can be quenched with excess of ethyl vinyl ether (EVE). Second block: after the first block preparation, 100 μL of a freshly prepared stock solution (0.686 M) of monomer **Nb-Br** (**M2**) (26.2 mg, 6.86 × 10^{-5} mol, 35 equiv) in anhydrous and degassed DCE was quickly added just above the top of the stirring polymerization mixture. Once all the monomer **M2** has been added, the reaction vial was capped, and the stirring at room temperature was continued for further 15 min. If only the brush diblock copolymer is desired, the polymerization can be quenched with an excess of EVE. Third block: after the complete conversion of the second monomer, 100 μL of a freshly prepared stock solution (0.279 M) of monomer **Nb-dye** (**M3**) (29.3 mg, 2.79 × 10^{-5} mol, 15 equiv) in anhydrous and degassed DCE was quickly added just above the top of the stirring polymerization mixture. Once all the monomer **M3** has been added, the reaction vial was capped and stirred at room temperature for 60 min until complete consumption of the monomer. The polymerization was quenched with a drop of EVE, and the reaction mixture was stirred for 15 min. The solvent was removed by rotary evaporation. The triblock brush copolymer was initially precipitated from DCM (~2 mL) into cold diethyl ether (~300 mL), filtered, and the solvent was removed *in vacuo*. This was repeated three times using a fresh volume of cold diethyl ether each time. Finally, the resulting solid was dissolved in 10 mL of acetone and dialyzed against 1 L of acetone for 48 h with a cellulose membrane tubing (MWCO 8000 Da). The solvent was refreshed multiple times. Once dialysis is completed, the contents of the dialysis tubing were filtered through a 0.45 μL PTFE syringe filter, and the solid was dried under high vacuum until constant weight. The pure brush triblock copolymer $(\mathbf{PNbPEG})_{50}$-*b*-$(\mathbf{PNbBr})_{40}$-*b*-$(\mathbf{PNbdye})_{12}$ was obtained as a fluffy dark blue solid. GPC data are provided in Table 1 and Figure S14. The ^{1}H NMR spectrum is given in Figure S79. The FT-IR spectrum is shown in Figure S80.

General Procedure for the Halide−Azide Exchange Reaction. Brush di- and triblock copolymers were functionalized with azides as follows. The synthesis of the azide-functionalized brush triblock copolymer $(\mathbf{PNbPEG})_{50}$-*b*-$(\mathbf{PNbN_3})_{40}$-*b*-$(\mathbf{PNbdye})_{12}$ is given as an example. A solution of purified bromide-functionalized BBCP $(\mathbf{PNbPEG})_{50}$-*b*-$(\mathbf{PNbBr})_{40}$-*b*-$(\mathbf{PNbdye})_{12}$ (300 mg) in anhydrous DMF (1 mL) was degassed by three freeze−pump−thaw cycles. The Schlenk flask was backfilled with argon, and sodium azide (NaN_3, 5 equiv relative to the moles of bromide in the polymer) was added. The flask was placed in an oil bath at 40 °C, and the reaction mixture was stirred for 48 h. After complete conversion of all side chain bromides to azides, as monitored by ^{1}H NMR and FT-IR spectroscopy, the reaction mixture was diluted with deionized water (5 mL), transferred to a cellulose membrane bag (MWCO 3500 Da) and stirred against deionized water for 48 h to remove excess of NaN_3 and DMF. The solvent was refreshed multiple times. After removal of the solvent under high vacuum, the azide-functionalized brush copolymer $(\mathbf{PNbPEG})_{50}$-*b*-$(\mathbf{PNbN_3})_{40}$-*b*-$(\mathbf{PNbdye})_{12}$ was obtained as a fluffy dark blue powder. GPC data are provided in Table 1 and Figure S17. The ^{1}H NMR spectrum is given in Figure S83. The FT-IR spectrum is shown in Figure S84.

General Procedure for the SPAAC Reaction. Brush di- and triblock copolymers were functionalized with PPT as follows. The azide-functionalized brush triblock copolymer $(\mathbf{PNbPEG})_{50}$-*b*-$(\mathbf{PNbPPT})_{40}$-*b*-$(\mathbf{PNbdye})_{12}$ is given as an example. The azide-functionalized BBCP $(\mathbf{PNbPEG})_{50}$-*b*-$(\mathbf{PNbN_3})_{40}$-*b*-$(\mathbf{PNbdye})_{12}$ (0.1 g) and the compound BCN-PPT (12) (1.3 equiv. relative to the moles of azide in the polymer) were dissolved in DCM (1 mL) and stirred for 36 h at room temperature in the dark. Dialysis using a cellulose membrane tubing (MWCO 3500 Da) in acetone for 36 h and in water for additional 48 h, followed by removal of the solvent under high vacuum in the dark provided the pure drug-functionalized BBCP $(\mathbf{PNbPEG})_{50}$-*b*-$(\mathbf{PNbPPT})_{40}$-*b*-$(\mathbf{PNbdye})_{12}$. GPC data are provided in Table 1 and Figure S19. The ^{1}H NMR spectrum is given in Figure S87. The FT-IR spectrum is shown in Figure S88.

General Procedure for the Self-Assembly of BBCPs. Polymeric micelles were prepared by a nanoprecipitation process, followed by the membrane dialysis method. In brief, a solution of the BBCP in acetone (1 mL) at a concentration of 5 mg mL^{-1} was added dropwise into 5 mL of 0.01 M PBS (pH 7.4) under vigorous stirring to give a final concentration of the polymer of 1 mg mL^{-1}. The mixture was stirred for approximately 30 min and then further dialyzed against the buffered solution for 48 h at room temperature. The medium was replaced every 2 h for the first 8 h and then replaced every 8 h. The micellar solution was filtered through a 0.45 μm syringe filter to remove aggregated particles. The filtrate was lyophilized, and the resulting powder was stored in a fridge until further experiments.

General Procedure for the Self-Assembly of BBCPs Encapsulating PTX. Polymeric micelles encapsulating PTX were prepared using the same procedure described above, with one modification. Briefly, PTX and the corresponding BBCP were dissolved in acetone (1 mL) at concentrations of 1.5 and 5 mg mL^{-1}, respectively, and this organic solution was added dropwise into 1 mL of 0.01 M PBS (pH 7.4) under vigorous stirring to give a final concentration of the polymer of 1 mg mL^{-1} and a final concentration of PTX of 0.3 mg mL^{-1}. The mixture was further stirred for around 30 min and then dialyzed against the buffered solution for 48 h at room temperature, with the medium refreshed as aforementioned. The micellar solution was filtered through a 0.45 μm syringe filter to remove aggregated particles or any insoluble PTX (non-encapsulated). The filtrate was lyophilized, and the resulting powder was stored in a fridge until further experiments.

Drug Loading and Encapsulation Efficiencies. The quantification of PTX encapsulated in the micelles was determined in triplicate by high-performance liquid chromatography (HPLC, Shimadzu), using a reverse phase C18 column (4.6 × 250 mm, 5 μm particle size). PTX was measured at 227 nm using a mobile phase consisting of a mixture of acetonitrile and water (3:1, v/v) at a flow rate of 1.0 mL min^{-1}. For each measurement, 100 μL of solution of PTX-loaded micelles previously prepared (with a final concentration of the polymer of 1 mg mL^{-1} and a target concentration of PTX of 0.3 mg mL^{-1}) was dissolved in 0.9 mL of acetonitrile under vigorous vortexing. The concentration of PTX was determined by using a standard curve of pure PTX solutions (1.5−10 mM) in acetonitrile and water (3:1, v/v). The results are given as mean ± standard deviation (SD) based on three independent measurements. A solution of PTX-free micelles was prepared following the same procedure and used to measure the presence of a background signal.

The loading content (LC) and encapsulation efficiency (EE) of PTX in the micelles were defined according to the following equations

$$\text{LC (\%)} = \text{weight of PTX encapsulated in micelles} / \text{total weight of PTX-loaded micelles} \times 100 \quad (1)$$

$$\text{EE (\%)} = \text{weight of PTX encapsulated in micelles} / \text{total weight of PTX originally added} \times 100 \quad (2)$$

***In Vitro* Stability Study.** To assess the stability of the micelles under different conditions, the changes in their hydrodynamic diameters were monitored over time. The micelles (1 mg mL^{-1}) were incubated under mildly acidic (0.1 M acetate buffer, pH: 5.5)

https://doi.org/10.1021/acs.biomac.1c01196
Biomacromolecules 2021, 22, 5290−5306

and physiological (0.01 M PBS buffer, pH: 7.4, and RPMI containing 10% FBS, pH: 7.4) conditions at 37 °C with constant gentle stirring. At pre-designed time intervals, aliquots were withdrawn from the solutions, and the hydrodynamic diameter was measured by DLS analysis. The results are given as mean ± SD based on three independent measurements.

***In Vitro* Drug Release Study.** The drug release profiles were evaluated in either neutral (0.01 M PBS buffer, pH: 7.4) or acidic (0.1 M acetate buffer, pH: 5.5) conditions as follows: micelles were dissolved in the buffered solution (1 mg mL^{-1}) and placed in a dialysis bag (MWCO: 8,000). Then, the whole bag was immersed in 50 mL of the same buffer solution and kept under gentle stirring at 37 °C. At specified time intervals, an aliquot was withdrawn from each different system and replenished with an equal volume of the fresh buffer solution to maintain an equal total volume. Quantification of PTX released was performed by RP-HPLC with detection at 227 nm, whereas 4-HOPPT was quantified by UV−vis spectroscopy at 325 nm; based on pre-plotted calibration curves. The release profile of the drug from the micelles was obtained by plotting cumulative drug release versus time.

Cell Culture Methods. The human MCF-7 (breast cancer), MCF-10A (normal breast), MDA-MB-231 (metastatic breast cancer), PC3 (prostate cancer), and PNT2 (normal prostate) cell lines were cultured in RPMI-1640 culture medium supplemented with 10% FBS and 1% antibiotics (penicillin at 100 U mL^{-1} and streptomycin at 100 $\mu g\ mL^{-1}$). Cells were cultured at 37 °C under a 5% CO_2 humidified atmosphere, and the culture medium was changed every 2−3 days. When the cell monolayer from each culture flask reached about 80% confluency, the adhered cell lines were detached with 0.25% trypsin−EDTA solution and homogenously distributed into the wells of the 96-well culture plates. All cell lines were purchased from Rio de Janeiro Cell Bank.

***In Vitro* Cytotoxicity Assay.** The cellular viability of micelles was evaluated using the CCK-8 assay according to the manufacturer's instructions. Briefly, cells were seeded in a 96-well plate at a density of 7500 cells per well in 200 μL of cell culture medium and incubated at 37 °C in a humidified atmosphere with 5% CO_2 for 24 h. Then, the medium was replaced by a fresh one (200 μL per well) containing various concentrations of different drug-conjugated and drug-loaded micelles (PPT/AB, PPT/ABC, PTX@AB, and PTX@ABC micelles), and the cells were incubated for further 48 h under the same cell culture conditions. Afterward, 10 μL of CCK-8 solution was added to each well, followed by incubation for another 3 h. The absorbance of the solution in each well was determined at a wavelength of 450 nm using a multi-well plate reader (FlashScan 530 Analytik Jena). The negative control was designated as untreated cells, which exhibited a cell viability of 100%. The cytotoxicity of free PPT and PTX, used as positive controls, as well as of blank micelles was evaluated in the same manner. The half-maximal inhibitory concentration (IC_{50}) values, expressed as mean ± SD, and their 95% confidence intervals (CI = 95%) from at least two different experiments carried out in triplicate were obtained by nonlinear regression using the GraphPad Prism 5.0 (GraphPad Software Inc.).

Cellular Uptake Assay. Confocal laser scanning microscopy (CLSM) was employed to observe the internalization of NIR fluorescent polymeric micelles into cells. MCF-7, PC3, and MCF10A cells were separately seeded on glass cover slides inside the wells of six-well plates at a density of 3×10^5 cells/well in 3 mL of complete growth culture medium. After incubation for 24 h at 37 °C in a humidified atmosphere with 5% CO_2, the cells were treated with non-cytotoxic concentrations of the polymeric micelles and incubated for further 8 and 24 h. After the incubation period, the growth medium was removed, and cells were gently washed three times with 1× PBS, fixed with 1× PBS containing 4% *p*−formaldehyde for 15 min at room temperature, and washed again with 1× PBS. Afterward, fixed cells were permeabilized with 1× PBS containing 0.2% Triton X-100 for 5 min, washed with 1× PBS, and incubated with Hoechst 33342 to stain the nuclei and with Alexa Fluor 555 Phalloidin for labeling the actin, according to instructions provided by the manufacturer. Finally, the slides containing the cells were rinsed once again with 1× PBS and mounted with one drop of the antifade reagent Prolong (Invitrogen). The fluorescence images were acquired using an Upright LSM780−NLO Zeiss confocal laser scanning microscope equipped with 405, 458, 488, 514, 561, and 633 nm laser excitation sources. The experiments were performed using an oil-immersion objective EC Plan-Neofluar 40×/1.30 Oil DIC. Hoechst 33342 was excited at 405 nm and emitted at 410−487 nm, whereas 561 nm laser and 568−639 nm were used to excite and emit Alexa Fluor 555 Phalloidin, respectively. The NIR fluorescent micelles were excited using a 633 nm laser, and its fluorescence was measured at 661−759 nm.

Statistic Analysis. All experimental data were repeated three times and are expressed as the mean ± SD. One-way analysis of variance (ANOVA) followed by the Tukey's post-test was performed to evaluate the differences in parameters across groups, with $p < 0.05$ as significantly different.

RESULTS AND DISCUSSION

Design and Synthesis of Monomers. We designed three different monomers incorporating (i) a PEG chain to confer water solubility, biocompatibility, and neutral surface charge to the nanoparticle, (ii) a NIR fluorescent cyanine dye to be used as an imaging agent of the nanocarrier, and (iii) a primary alkyl bromide to allow easy further functionalization such as the attachment of an anticancer compound. We have chosen *exo*-norbornene-derived imides as monomers to generate the BBCPs because of their known fast polymerization kinetics, easy functionalization, and absence of irreversible chain-transfer, which allows for living ROMP.[65,66]

cis-5-Norbornene-*exo*-2,3-dicarboxylic anhydride (**1**), the common precursor for the monomers **M1** (Scheme 1), **M2**

Scheme 1. Synthetic Routes Employed for the Preparation of Monomers Nb-PEG (M1) and Nb-Br (M2)

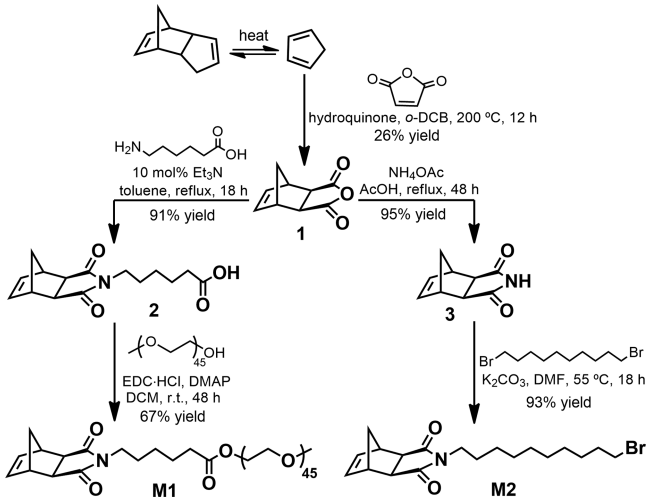

(Scheme 1), and **M3** (Scheme 2), was prepared by a Diels−Alder reaction of commercial cyclopentadiene and maleic anhydride at 200 °C followed by multiple recrystallizations (5×) from boiling toluene.[67] Isolation of the *exo*-isomer **1** from the *exo/endo* mixture, in 26% yield, was essential to maintain stereochemistry throughout the steps to monomers **M1**, **M2**, and **M3**. *Exo*-monomers have shown faster reaction times, higher conversion rates, and better control of ROMP compared to the *exo/endo* mixture or *endo*-form.[66,68]

Macromonomer **Nb-PEG (M1)** was synthesized in two steps from **1** following a literature procedure[69] starting with the preparation of carboxylic acid **2**, in 91% yield. EDC-mediated

https://doi.org/10.1021/acs.biomac.1c01196
Biomacromolecules 2021, 22, 5290−5306

Scheme 2. Synthetic Route Employed for the Preparation of NIR Fluorescent Monomer Nb-Dye (M3)

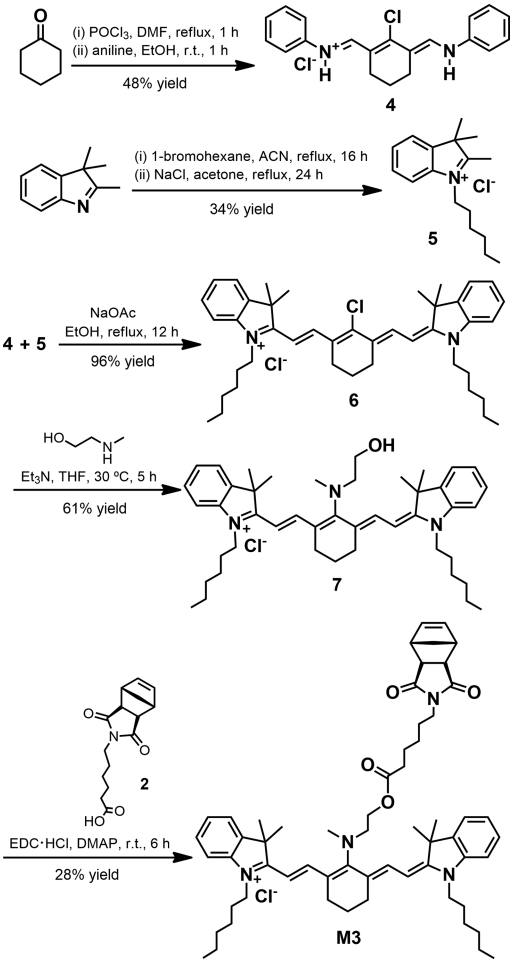

esterification of **2** with commercially available PEG methyl ether (M_n = 2000 Da) yielded the macromonomer **Nb-PEG** in 67% yield (Scheme 1).

Considering that the Grubbs' third-generation initiator (**G3**) is incompatible with azides and alkynes,[70] we synthesized monomer **Nb-Br** (**M2**) carrying an alkyl bromide for facile conversion to azide in a post-ROMP modification step. We incorporated a ten-carbon spacer between the strained norbornene moiety and the terminal bromide to reduce steric hindrance between the growing polymer chain and the branched side chains during ROMP and to facilitate subsequent post-ROMP functionalization. Monomer **M2** was obtained in two steps from **1** (Scheme 1) through nucleophilic addition−elimination of **1** using ammonium acetate affording the corresponding imide **3** in 95% yield. Subsequently, compound **3** was converted to the alkyl halide **M2**, in 93% yield, through a *N*-alkylation reaction with 1,10-dibromodecane in DMF in the presence of potassium carbonate.

We have designed the BBCPs to include a short block containing a NIR dye that allows for the direct visualization of the nanosystem inside cells. We focused on the synthesis of a dye from the tricarbocyanine family because this class of compounds has demonstrated strong fluorescence in the NIR region, high photostability, and low cytotoxicity, making them ideal NIR probes.[71−75] The five reactions employed for the synthesis of the monomer **Nb-dye** (**M3**) are outlined in Scheme 2.

The preparation of the iminium salt **4** involved the Vilsmeier−Haack formylation of cyclohexanone. The Vilsmeier−Haack reagent was generated from phosphorus(V) oxychloride and *N*,*N*-dimethylformamide, which reacted in excess with cyclohexanone, giving an iminium intermediate. Hydrolysis of this intermediate provided a dialdehyde, which was further transformed into iminium salt **4** by treatment with aniline. In parallel, the indolenium derivative **5** was prepared by *N*-alkylation of commercially available 2,3,3-trimethylindolenine with 1-bromohexane in refluxing acetonitrile, followed by refluxing with excess of sodium chloride to substitute the counterion. The condensation of the quaternary ammonium salts **4** and **5** carried out under refluxing ethanol in the presence of anhydrous sodium acetate afforded the *meso*-chloro heptamethine cyanine dye **6** as a bright-green solid in 96% yield.

Studies have shown that the presence of a rigid carbocyclic ring in the heptamethine chain enhances the photostability and fluorescence quantum yield, as well as decreases aggregation of the dye in solution.[76,77] Furthermore, the *meso*-chlorine substituent in the cyclohexene ring provides a reactive site for the fluorophore moiety, allowing for easy functionalization with various nucleophiles.[75,78] The chlorine in the heptamethine cyanine dye **6** was displaced upon treatment with 2-methylaminoethanol to form the *meso*-*N*-methylethanolamino-substituted cyanine dye **7** as a dark-blue solid, in 61% yield. Dye **7** was characterized by ^{1}H NMR spectroscopy (Figures S1b and S66) through the presence of the new triplet signals at 4.04 and 3.93 ppm assigned to the methylene groups of the *N*-methylethanolamine moiety, as well as a singlet at 3.53 ppm corresponding to the hydrogens of the methyl group adjacent to the nitrogen atom. The formation of dye **7** was further confirmed by ^{13}C NMR spectroscopy (Figure S67) and by mass spectrometry (ESI-QTOF-MS) by its molecular ion peak $[M]^+$ at 662.5021 m/z (calcd For $C_{45}H_{64}N_3O$ = 662.5043 m/z).

The final synthetic step shown in Scheme 2 involved the EDC-mediated coupling of the norbornene precursor **2** with the dye **7**. Purification of the monomer containing the *meso*-amino-derivatized cyanine dye (**Nb-dye**, **M3**) was achieved by extraction into dichloromethane and column chromatography on silica gel. The desired monomer **Nb-dye** has been isolated in high purity as confirmed by ^{1}H and ^{13}C NMR spectroscopies (Figures S68 and S69). The ^{1}H NMR spectrum of **Nb-dye** (Figures S1c and S68) showed the characteristic signals of the norbornene: δ = 6.20 ppm (H_s), 3.16 ppm (H_t), 2.58 ppm (H_u), 1.42−1.37 ppm ($H_{a'}$), and 1.10 ppm ($H_{b'}$), as well as signals assigned to the protons of the fluorophore moiety and linker. The methylene protons "H_r" at 4.35 ppm shifted downfield in comparison to the corresponding ones of dye **7** (at 4.04 ppm), supporting the successful coupling reaction. Monomer **Nb-dye** was further characterized using mass spectrometry (ESI-QTOF-MS) by its molecular ion peak $[M]^+$ at 921.6216 m/z (calcd for $C_{60}H_{81}N_4O_4$ = 921.6252 m/z). See the Supporting Information for the synthesis and characterization of all compounds presented in Schemes 1 and 2.

Synthesis of the Clickable Bioactive Derivative. The preparation of the clickable derivative (**12**, BCN-PPT) of the natural product piplartine (**8**, PPT) is outlined in Scheme 3. 4-Hydroxypiplartine (**9**, 4-HOPPT) was synthesized in five

https://doi.org/10.1021/acs.biomac.1c01196
Biomacromolecules 2021, 22, 5290−5306

Scheme 3. Synthesis of Clickable PPT Derivative BCN-PPT (12)

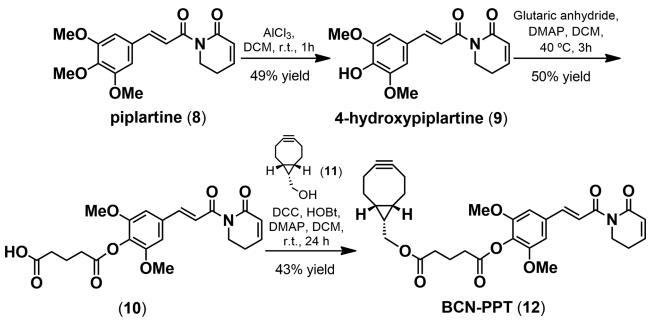

steps, according to methodologies previously described by our group.[54,79] We have chosen to modify the 4-hydroxy derivative of PPT because it enables the conjugation of linkers or other moieties to its structure in a simple and versatile way without compromising any essential residue for the PPT antitumor activity. The hydroxyl group in **9** was esterified to the carboxylic acid **10** in moderate yield (50%) through the opening of glutaric anhydride in the presence of catalytic amounts of DMAP in dichloromethane (DCM) under reflux.

The synthesis of derivative **12** was accomplished in moderate yield (43%) by the Steglich esterification of carboxylic acid **10** with commercial (1*R*,8*S*,9*S*)-bicyclo[6.1.0]-non-4-yn-9-ylmethanol (BCN−OH, **11**) in the presence of 1-hydroxybenzotriazole (HOBt) as the *N*-acylurea—suppressing additive in addition to DCC and DMAP in the dark. Compound **12** was characterized by ^{1}H and ^{13}C NMR spectroscopy (Figures S74 and S75) and HRMS. The presence of a hydrolytically labile ester linker between the bioactive PPT moiety and the cyclooctyne partner was included due to its susceptibility to cleavage in the biological environment. We hypothesize that the cleavable ester linkage would undergo enzymatic hydrolysis, releasing the anticancer compound 4-HOPPT (**9**) from the nanocarrier in diseased regions.

Design and Synthesis of Amphiphilic BBCPs via ROMP. To generate the desired amphiphilic BBCPs with a precise molecular weight (MW) and unimodal MW distribution, we first screened a series of conditions to be used in the ROMP reactions. The living character of the ROMP of monomers **Nb-Br** (**M2**) and **Nb-dye** (**M3**), and their polymerization times were investigated through kinetic studies using *in situ* ^{1}H NMR spectroscopy. These kinetic experiments were conducted at constant initial monomer concentration with the initiator **G3**, in 1,2-dichloroethane (DCE) at room temperature, and monomer conversions were monitored by the disappearance of the resonance corresponding to the olefinic protons of the norbornene (at 6.3−6.1 ppm) and simultaneous appearance of broad olefinic signals (at 5.9−5.2 ppm) assigned to the brush polymer.

According to the ^{1}H NMR spectra shown in Figures S2b−S4b, as well as data in Figures S2c−S4c, all monomers polymerized quantitatively within 45 min for **Nb-PEG** (**M1**), 15 min for **Nb-Br** (**M2**), and 60 min for **Nb-dye** (**M3**). Figures

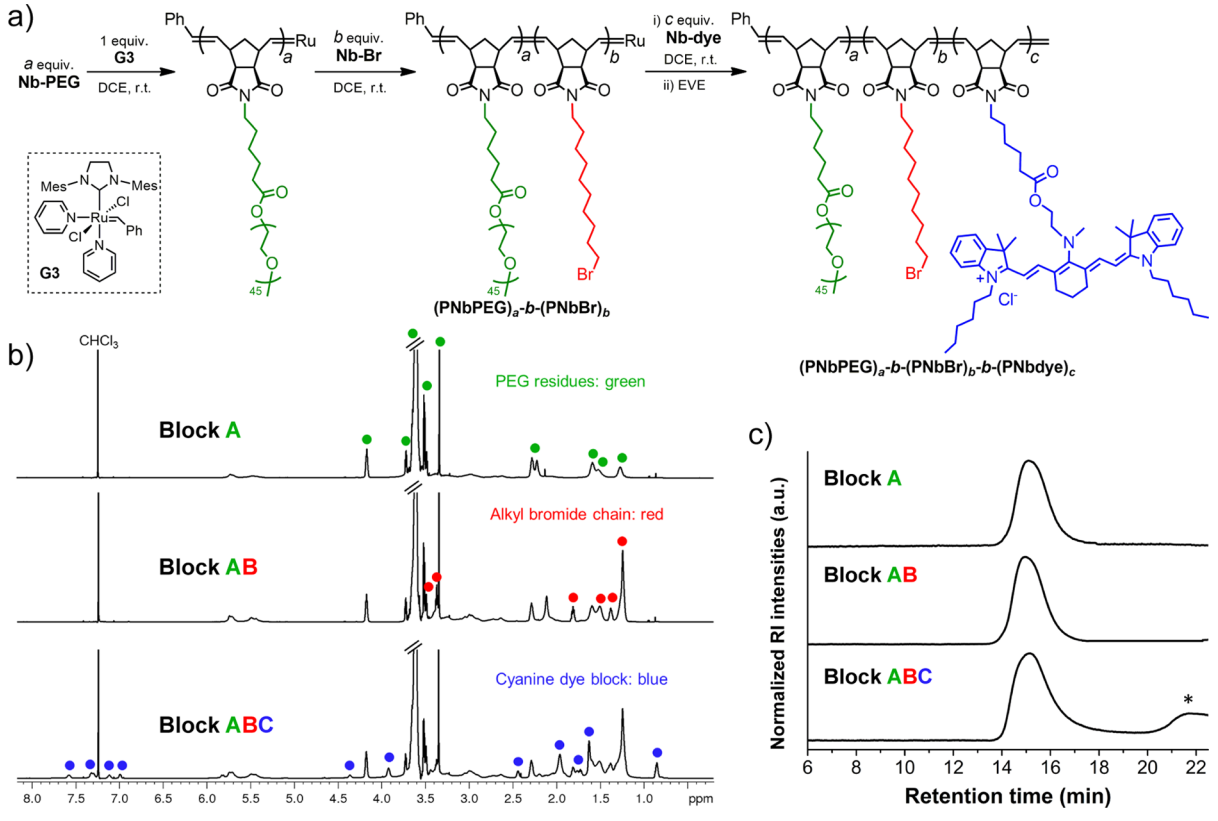

Figure 2. (a) Schematic representation of the synthesis of amphiphilic BBCPs by sequential graft-through ROMP reactions. (b) ^{1}H NMR spectra of the brush homopolymer $(\mathbf{PNbPEG})_{50}$ (Block A), the diblock $(\mathbf{PNbPEG})_{50}$-*b*-$(\mathbf{PNbBr})_{40}$ (Block AB), and the final BBCP $(\mathbf{PNbPEG})_{50}$-*b*-$(\mathbf{PNbBr})_{40}$-*b*-$(\mathbf{PNbdye})_{12}$ in $CDCl_3$ (600 MHz). Green dots correspond to PEG resonance signals, red dots correspond to the alkyl bromide chain signals, and blue dots represent signals from the cyanine dye block. (c) GPC traces showing the step-by-step formation of $(\mathbf{PNbPEG})_{50}$-*b*-$(\mathbf{PNbBr})_{40}$-*b*-$(\mathbf{PNbdye})_{12}$. * indicates the peak corresponding to small amounts of unconverted monomer.

https://doi.org/10.1021/acs.biomac.1c01196
Biomacromolecules 2021, 22, 5290−5306

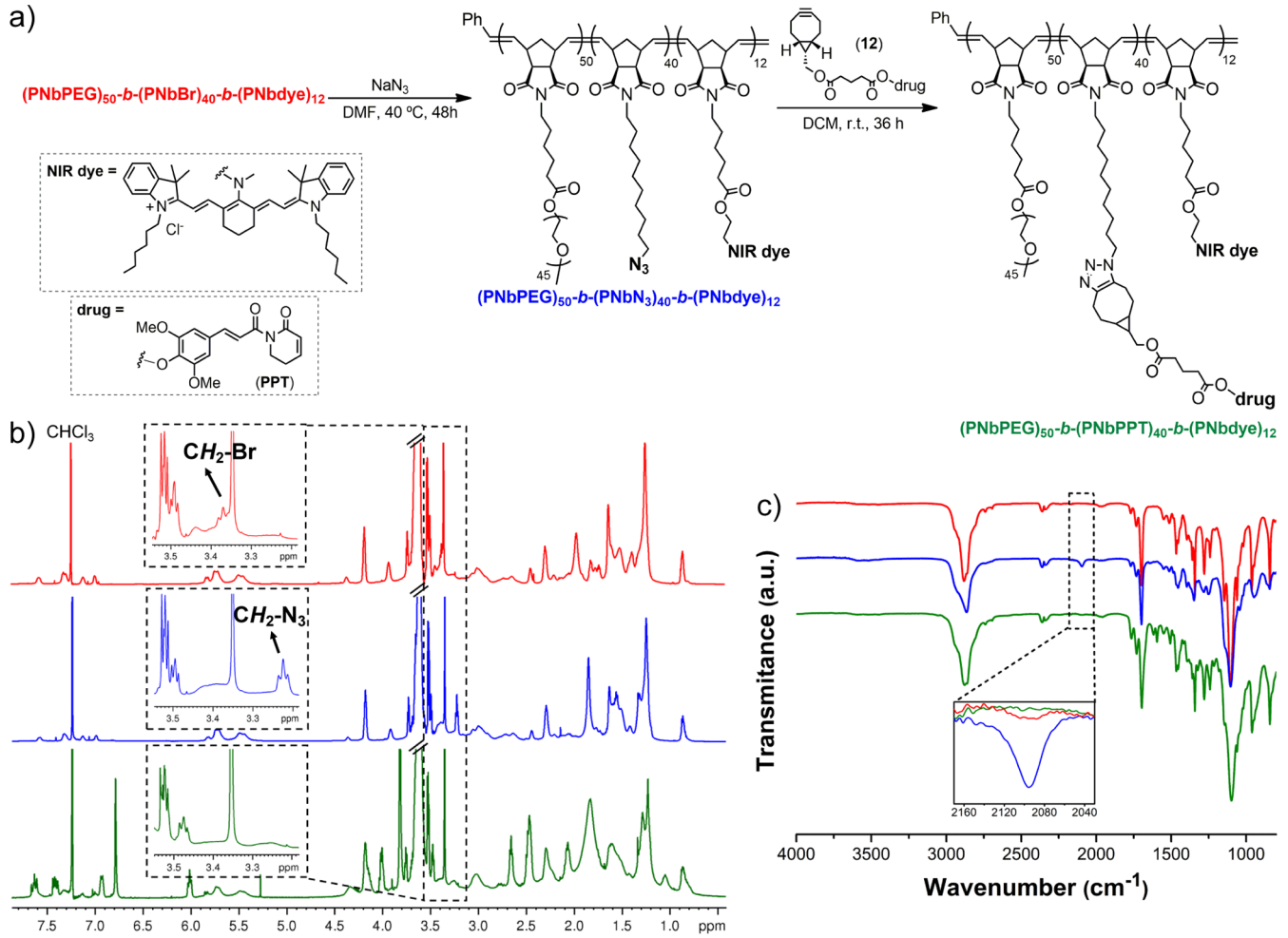

Figure 3. (a) Schematic representation of the synthesis of BBCP-drug conjugates via *post*-ROMP functionalization (bromide−azide substitution followed by SPAAC reaction). (b) ^{1}H NMR spectra and (c) FT-IR spectra comparing the corresponding bromide- ((**PNbPEG**)$_{50}$-*b*-(**PNbBr**)$_{40}$-*b*-(**PNbdye**)$_{12}$, red traces), azide- ((**PNbPEG**)$_{50}$-*b*-(**PNbN$_3$**)$_{40}$-*b*-(**PNbdye**)$_{12}$, blue traces), and drug-functionalized ((**PNbPEG**)$_{50}$-*b*-(**PNbPPT**)$_{40}$-*b*-(**PNbdye**)$_{12}$, green traces) BBCPs.

S2d−S4d demonstrate the first-order kinetics and excellent molecular weight control provided by ROMP with **G3**, confirming their living character with the absence of chain transfer and chain termination.

Taking into consideration the polymerization behavior of all monomers, a series of amphiphilic BBCPs (Table 1: entries 1−10) were synthesized via one-pot two- or three-step sequential ROMP of hydrophilic macromonomer **Nb-PEG** (**M1**) and hydrophobic monomers **Nb-PEG** (**M1**), **Nb-Br** (**M2**) and **Nb-dye** (**M3**) initiated by **G3** at room temperature (Figure 2a). The effect of several parameters on the properties of the final BBCPs was investigated, including the molar feed ratios of monomers to the catalyst, solvent polarity, and order of block sequences, and the results are summarized in Table 1.

Studies have shown the significant effect that different solvents have on the polymerization rates of ruthenium catalysts and, consequently, on the polymer characteristics.[70] The three monomers and **G3** are soluble in DCM and DCE, which are among the preferred solvents for ROMP. As weak polar solvents, they can promote the ligand dissociation and act as non-coordinating solvents. Table 1 shows that changing the solvent from DCM (ε = 9.1) to DCE (ε = 10.4) has no significant effect. In all cases, monomer conversions are higher than 95%, and the polymers have experimental M_n values comparable to the theoretical ones. Slightly lower $Đ$ values were observed in DCE in comparison to DCM, which is probably related to the faster initiation observed in more polar solvents.[70]

When a sequential hydrophilic/hydrophobic molar feed ratio of around 50:50 was employed (assuming [**G3**] = 1 equiv), the resulting AB brush diblock copolymer (**PNbPEG**)$_{50}$-*b*-(**PNbBr**)$_{48}$ (**BBCP7**) exhibited low dispersity, and a monomodal trace is displayed in the GPC chromatogram (Figure S5b). The number-average degree of polymerization ($DP_{n,GPC}$) and number-average molecular weight ($M_{n,GPC}$) values obtained by GPC were found to be in agreement with the theoretical ones. The small difference between these values can be attributed to different physico-chemical characteristics of the highly branched polymer studied in comparison to the linear poly(styrene) (PS) standards used for GPC calibration. ^{1}H NMR spectra (Figure S5c) confirmed that the sequential addition of monomers proceeded with their sequential incorporation into each block. The experimentally determined $DP_{n,NMR}$ (obtained from the integrated ^{1}H NMR spectrum shown in Figure S77) was then used to calculate the $M_{n,NMR}$, which was again very close to the theoretical value (Table 1). The *in vitro* studies were conducted by using the BBCP

https://doi.org/10.1021/acs.biomac.1c01196
Biomacromolecules 2021, 22, 5290−5306

Table 2. Characterization Data of Self-Assembled Micelles Based on BBCPs with and without PTX[a,b]

micelle name	BBCP composition	size[c] (nm)	PDI[c]	ζ-potential[c] (mV)	LC[d] (%)	EE[e] (%)
blank@AB	$(PNbPEG)_{50}$-*b*-$(PNbBr)_{48}$	38 ± 19	0.26	−2.1 ± 0.8		
PPT/AB	$(PNbPEG)_{50}$-*b*-$(PNbPPT)_{48}$	52 ± 31	0.35	−1.5 ± 0.5	9.7[f]	
PTX@AB	$(PNbPEG)_{50}$-*b*-$(PNbBr)_{48}$	89 ± 39	0.20	−2.1 ± 0.3	22 ± 0[g]	93 ± 1[g]
blank@ABC	$(PNbPEG)_{50}$-*b*-$(PNbBr)_{40}$-*b*-$(PNbdye)_{12}$	48 ± 30	0.39	−1.5 ± 0.7		
PPT/ABC	$(PNbPEG)_{50}$-*b*-$(PNbPPT)_{40}$-*b*-$(PNbdye)_{12}$	80 ± 42	0.28	−0.9 ± 0.4	7.9[f]	
PTX@ABC	$(PNbPEG)_{50}$-*b*-$(PNbBr)_{40}$-*b*-$(PNbdye)_{12}$	102 ± 53	0.27	−1.9 ± 0.7	22 ± 0[g]	94 ± 1[g]

[a]Abbreviations: PDI = polydispersity index; LC = loading content; EE = encapsulation efficiency. [b]In 0.01 M PBS (pH 7.4). [c]Determined using DLS analysis. [d]LC (wt %) = (weight of the drug in the micelles/weight of drug-loaded micelles) × 100. [e]EE (wt %) = (weight of PTX in the micelles/weight of PTX in feed) × 100. [f]Determined by ^{1}H NMR spectroscopy. [g]Determined using RP-HPLC measurements. Each value is expressed as mean ± SD from three independent measurements.

$(PNbPEG)_{50}$-*b*-$(PNbBr)_{48}$ as the representative brush diblock copolymer.

Concomitantly, ABC and BAC triblock brush copolymers were also synthesized employing sequential copolymerization of the monomers **Nb-PEG**, **Nb-Br**, and **Nb-dye** (Figure 2a). The $Đ$ values for ABC and BAC BBCPs were 1.70 and 1.90 (Table 1), respectively. Considering the lower dispersity obtained for $(PNbPEG)_{50}$-*b*-$(PNbBr)_{40}$-*b*-$(PNbdye)_{12}$ (**BBCP9**), which is an important parameter for drug delivery systems, we have chosen it as the representative brush triblock copolymer for subsequent studies. Step-by-step analysis of the ^{1}H NMR spectra along the growth of the polymeric chain (Figure 2b) indicated the presence of typical signals of the PEG chain at δ 3.72−3.48 ppm (−OCH_2CH_2O−), alkyl bromide chain at δ 3.37 ppm (−CH_2Br), and cyanine dye moiety at δ 7.58−6.99 ppm (aromatic H), providing evidence of the successful formation of the desired BBCP $(PNbPEG)_{50}$-*b*-$(PNbBr)_{40}$-*b*-$(PNbdye)_{12}$. ^{1}H NMR spectroscopy also revealed high monomer conversions. For the first and second blocks, the measured $M_{n,GPC}$ was similar to the theoretically expected ones; however, the experimental $M_{n,GPC}$ after incorporation of the third block was underestimated in comparison to the theoretical $M_{n,theor.}$ value. We hypothesize that this is due to strong interactions between the GPC column and the polymer, in particular the block containing the cyanine dye. Thus, the DP_n of each block of the ABC polymer was estimated by assuming complete monomer conversion of **Nb-PEG** (**M1**) (as observed by GPC and ^{1}H NMR spectroscopy) and then comparing the integrals of the peaks at 3.37 ppm (−CH_2Br of the second block) and 7.58 ppm ($H_{aromatic}$ of the third block) to those at 3.61 ppm of PEG methylene protons (Figure S79); close agreement between the theoretical and the experimentally measured block composition was observed (Table 1).

Synthesis of Azide-Functionalized BBCPs via Bromide−Azide Substitution. Following ROMP, we carried out a *post*-polymerization bromide−azide exchange reaction to generate the azide-functionalized BBCP $(PNbPEG)_{50}$-*b*-$(PNbN_3)_{40}$-*b*-$(PNbdye)_{12}$, as illustrated in Figure 3a. The same methodology was employed for the synthesis of $(PNbPEG)_{50}$-*b*-$(PNbN_3)_{48}$.

Spectroscopic analysis (^{1}H NMR and FT-IR) of the obtained azide-functionalized di- and triblock BBCPs was used to demonstrate the successful conversion of the pendant bromides into azides. The ^{1}H NMR spectrum of $(PNbPEG)_{50}$-*b*-$(PNbBr)_{40}$-*b*-$(PNbdye)_{12}$ (red line in Figure 3b) shows a triplet peak at δ 3.37 ppm corresponding to the methylene hydrogens adjacent to the terminal bromide (CH_2Br). After substitution of the halides with azide groups, the signal at δ 3.37 ppm disappeared and a new triplet upfield appeared at δ 3.22 ppm (blue line in Figure 3b), which is assigned to the CH_2N_3 protons of $(PNbPEG)_{50}$-*b*-$(PNbN_3)_{40}$-*b*-$(PNbdye)_{12}$. In addition, the FT-IR spectrum of the polymer after the halide−azide exchange (blue traces in Figure 3c) show a new absorption band at 2096 cm^{-1}, which is characteristic of azide groups, confirming the successful generation of BBCP-N_3. The extent of azides incorporated into the copolymer was determined via ^{1}H NMR spectroscopy ($CDCl_3$, 600 MHz) from the comparison of peak integrations of the CH_2N_3 protons at δ 3.22 ppm with the methylene protons of PEG entity at δ 3.67−3.57 ppm (see the integrated ^{1}H NMR spectrum of BBCP-N_3 in the Supporting Information, Figure S83). The results indicate that the conversion of the pendant bromides into azides was quantitative. A similar spectroscopic analysis was also carried out for the corresponding brush diblock copolymers $(PNbPEG)_{50}$-*b*-$(PNbBr)_{48}$ and $(PNbPEG)_{50}$-*b*-$(PNbN_3)_{48}$ (Figures S77 and S81, respectively), which showed a quantitative generation of the azide-functionalized polymer.

Synthesis of Drug-Functionalized BBCPs via *Click* Chemistry. Copper-free strain-promoted akide−alkyne cycloaddition (SPAAC) was used to covalently attach the clickable derivative BCN-PPT (**12**) to the azide-functionalized BBCPs (Figure 3a). We employed SPAAC instead of the classical copper-catalyzed azide−alkyne cycloaddition (CuAAC) to avoid copper(I) contamination, which is a recognized cytotoxic element.[80−83] Moreover, this copper-free reaction has proven useful for the quantitative functionalization of nanomaterials with widespread bioapplications.[84]

Successful formation of the BBCP-PPT conjugates was first verified by FT-IR spectroscopy. FT-IR spectra were acquired at different time points to monitor the SPAAC coupling (see the final FT-IR spectra of the di- and triblock conjugates in the Supporting Information, Figures S86 and S88, respectively). The azide asymmetric stretching at 2096 cm^{-1}, present in the FT-IR spectrum of $(PNbPEG)_{50}$-*b*-$(PNbN_3)_{40}$-*b*-$(PNbdye)_{12}$ (blue traces in Figure 3c or Figure S84), is completely absent from the final drug-functionalized BBCP $(PNbPEG)_{50}$-*b*-$(PNbPPT)_{40}$-*b*-$(PNbdye)_{12}$ spectrum (green traces in Figure 3c, or Figure S88), suggesting the completion of the click reaction after 36 h.

According to ^{1}H NMR spectroscopy, the peak corresponding to the CH_2N_3 at δ 3.22 ppm disappeared, also indicating consumption of the azide after 36 h (green line in Figure 3b) . Additionally, functionalization of the BBCP is evidenced by the presence of peaks in the ^{1}H NMR spectrum originating from both the polymer and PPT portions. The integration ratio of the signal at δ 6.02 ppm, corresponding to an olefinic proton of

https://doi.org/10.1021/acs.biomac.1c01196
Biomacromolecules 2021, 22, 5290−5306

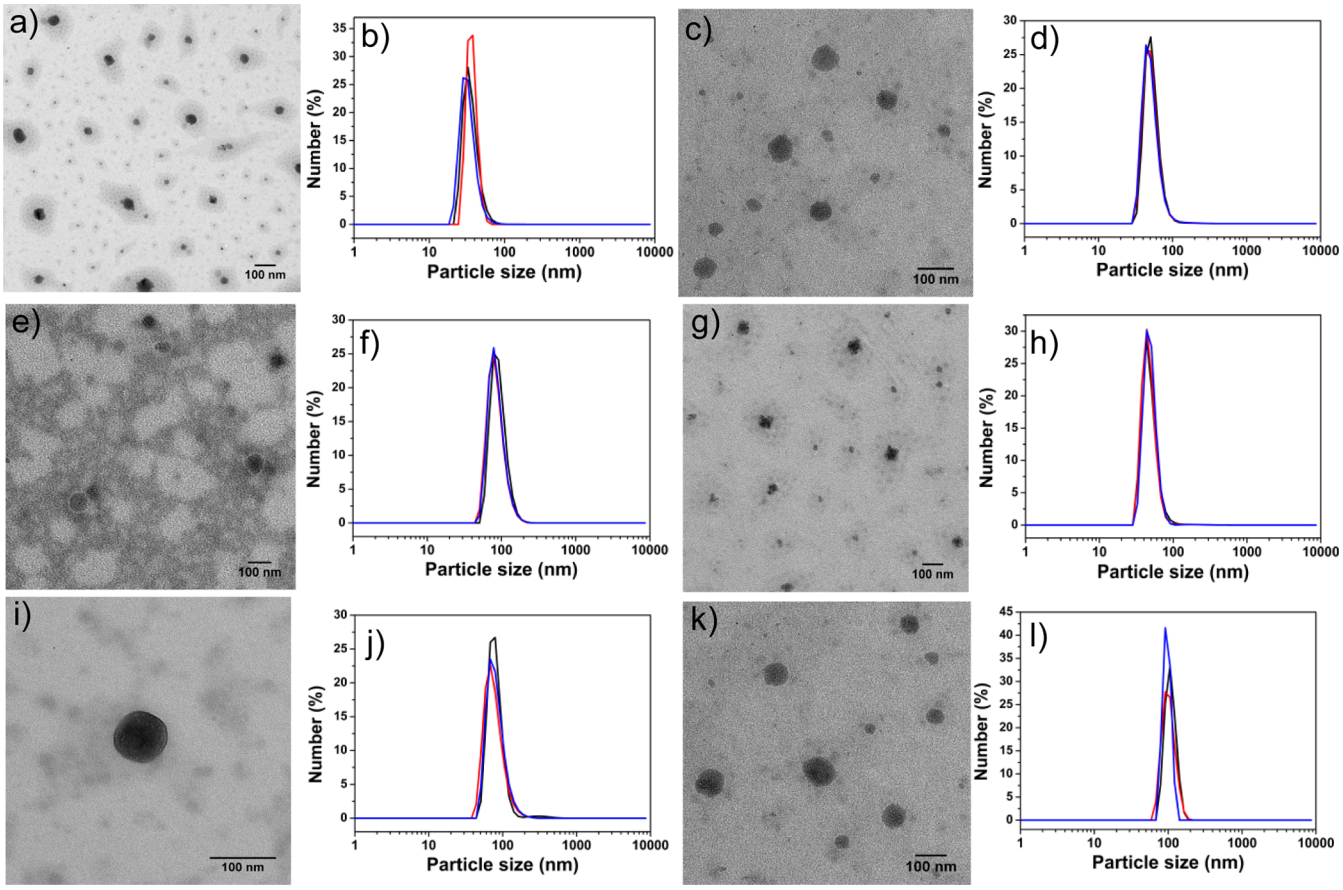

Figure 4. Representative TEM images and DLS size distribution curves of (a,b) blank@AB, (c,d) PPT/AB, (e,f) PTX@AB, (g,h) blank@ABC, (i,j) PPT/ABC, and (k,l) PTX@ABC assembled BBCP micelles in an aqueous medium. See Table 2 for more details. DLS results are presented in percentage by number and were collected in triplicate.

the PPT moiety, with respect to the signal of the methylene protons of the PEG chain ($-OCH_2CH_2O-$) at δ 3.67−3.57 ppm suggests the quantitative incorporation of the BCN-drug derivative into the BBCP (see integrated ^{1}H NMR spectra of the BBCP−PPT conjugates in the Supporting Information, Figures S85 and S87). Thus, $(\mathbf{PNbPEG})_{50}$-*b*-$(\mathbf{PNbPPT})_{40}$-*b*-$(\mathbf{PNbdye})_{12}$ has a $M_{n,NMR}$ of 160.6 kDa, with 7.9 wt % of PPT (Table 2). For $(\mathbf{PNbPEG})_{50}$-*b*-$(\mathbf{PNbPPT})_{48}$, $M_{n,NMR}$ is 156.7 kDa, with 9.7 wt % of PPT (Table 2).

Self-Assembly of BBCPs in Aqueous Media. An attractive feature of amphiphilic brush copolymers is their ability to behave as macrosurfactants even at very dilute concentrations. Owing to the amphiphilic nature of the synthesized BBCPs containing relatively long hydrophilic PEG side chains and short, similar length hydrophobic side chains, one can hypothesize that they spontaneously assemble in selected solvents into spherical micelles, as proposed by Rzayev and co-workers.[85]

We used nanoprecipitation followed by solvent exchange to induce assembly of the brush copolymers into micellar aggregates with a final concentration of 1 mg mL^{-1}. TEM and DLS analyses were utilized to characterize the formed micelles, and the results are summarized in Table 2. Morphological investigation of the self-assembled aggregates was carried out by TEM after dropping the aqueous solution onto carbon-coated copper grids, followed by drying at room temperature. As shown in Figure 4, TEM images confirmed that spherical nanosized micelles were obtained in all cases, suggesting that the high side chain asymmetry in the brush structure dictated their packing mode.[85]

The hydrodynamic diameter, size distribution, and ζ-potential of micelles in aqueous medium were determined by DLS analysis (Figure 4 and Table 2). The results show that the average size of the AB micelles, namely, blank@AB and PPT/AB micelles, is 38 ± 19 and 52 ± 31 nm, respectively, with polydispersity indices (PDI) of 0.26 and 0.35, which was smaller than their corresponding ABC micelles (blank@ABC micelles: size = 48 ± 30 nm, PDI = 0.39 and ABC/PPT micelles: size = 80 ± 42 nm, PDI = 0.28).

Since both AB and ABC micelles present an equal length of the hydrophilic PEG block, larger micelles were produced possibly due to the presence of the bulky cyanine dye moieties in the ABC micelles, which are expected to be in their core because of the increased hydrophobicity brought by the two C6-alkyl chains. Nanomaterials with hydrodynamic sizes of 10−200 nm can greatly reduce their kidney clearance, capture by the macrophages, and prolonged blood circulation, thereby accumulating at the tumor site through the EPR effect.[9]

The nanoscale size presented by the assembled micelles in aqueous solution allows them to be used as carriers for other hydrophobic anticancer compounds, such as the potent drug PTX. Thus, as a demonstration of the versatility of our nanosystems, we selected blank@AB and blank@ABC micelles to encapsulate PTX to evaluate the behavior of PTX-loaded micelles in *in vitro* cytotoxicity studies. During the micelle formation, PTX was encapsulated into the hydrophobic core.

https://doi.org/10.1021/acs.biomac.1c01196
Biomacromolecules 2021, 22, 5290−5306

The resulting micelles (PTX@AB and PTX@ABC) were spherical in nature (Figure 4e and 4k, respectively) with average sizes of 89 ± 39 and 102 ± 53 nm, respectively (Table 2, and Figure 4f and 4l, respectively). The average sizes of PTX-loaded AB and ABC micelles are larger when compared to their corresponding blank@AB and blank@ABC micelles, suggesting successful encapsulation of PTX. Furthermore, representative TEM images showed that encapsulation did not disturb the spherical micellar structures. High loading contents (LC) of 22% were obtained, as well as high encapsulation efficiencies (93% and 94%) for PTX@AB and PTX@ABC micelles, respectively. We suggest that these results can be attributed to the presence of hydrophobic interactions between the hydrophobic anticancer drug and the hydrophobic core.

According to ζ-potential measurements (Table 2), all micelles have a neutral surface charge, which is consistent with the dense outer PEG shell. Particles with low ζ-potential values (−10 to +10 mV) rapidly tend to aggregate. The steric stabilization provided by PEG chains, however, avoids micelle aggregation, as confirmed by DLS and TEM results (Figure 4).

The stability of the nanoformulations is a key parameter for their use in drug delivery applications. While nanosystems should be stable under physiological conditions to protect drugs from premature degradation and release, a stimuli responsive behavior, such as pH-responsiveness, is desirable to trigger the drug release when the nanosystem reaches the acidic tumor environment. We assessed the stability of our blank micelles under three different conditions at 37 °C: (i) 0.01 M PBS, pH 7.4, (ii) cell culture medium (RPMI) supplemented with 10% FBS, pH 7.4, and (iii) 0.1 M acetate buffer, pH 5.5, through monitoring their sizes over a period of three days, using DLS measurements. No significant changes in the average sizes of both micelles were observed in 0.01 M PBS solution (pH 7.4) during the 72 h (Figure 5a). Whereas a slight increase of around 10 nm in micelle size was observed in RPMI +10% FBS over the same period. These findings demonstrate the good colloidal stability of the micelles under physiological conditions, and the low tendency to aggregate even in a protein-enriched medium, likely due to the highly dense PEG surface coverage. The presence of PEG on the nanoparticle (NP) surfaces is well-recognized to shield the surface from aggregation, inhibiting nonspecific interactions with serum proteins and consequently reducing macrophage uptake, leading to a prolonging of the NP systemic circulation time.[9]

Incubation in 0.1 M acetate buffer (pH 5.5) mimicking the mildly acidic microenvironment of tumors and endosomal/lysosomal compartments resulted in an increase of around 25 nm in the hydrodynamic size of blank@ABC micelles over 48 h (Figure 5b). After 72 h, a more significant increase in size of approximately 65 nm was also observed. Aggregates with larger sizes and broader size distributions also emerged during these periods, indicating some disassembly in the nanosystem promoted by the weakly acidic pH and, thus, a pH-responsive character of these micelles in solution. Under such lower pH condition (pH 5.5), it can be hypothesized that the tertiary amines of the cyanine moiety in the hydrophobic block, for instance, are partially protonated and become positively charged, repelling each other in the hydrophobic core, thus leading to disentanglement of polymeric chains and consequent micelle disassembly in solution.

***In Vitro* Drug Release.** To simulate the drug release under biological conditions, the *in vitro* drug release profile of the

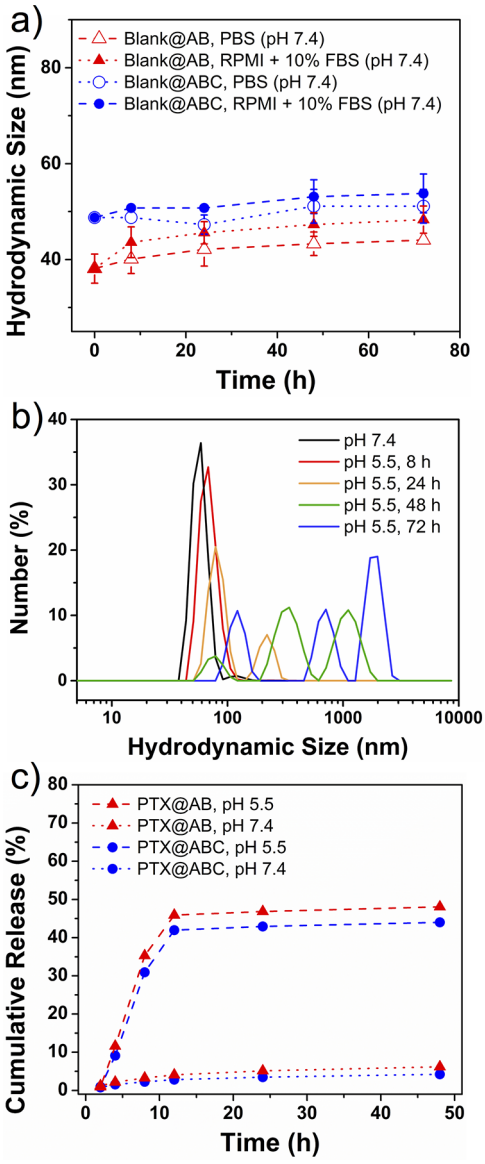

Figure 5. (a) Size changes of blank@AB and blank@ABC micelles over time under physiological conditions at 37 °C by DLS measurements. (b) Size changes of blank@ABC micelles over time at pH 5.5 at 37 °C by DLS measurements. (c) In vitro drug release profile of PTX from PTX@AB and PTX@ABC micelles at pH 5.5 and pH 7.4 at 37 °C during 48 h.

PPT-conjugated and PTX-loaded micelles over time upon exposure to mildly acidic and physiological buffered conditions at 37 °C was investigated. As depicted in Figure 5c, PTX@AB and PTX@ABC micelles displayed minimal PTX release (*ca* 5%) at 0.01 M PBS (pH 7.4), which can be attributed to the escape of weakly interacting PTX molecules in the core of the NPs. These results corroborate those obtained in the stability studies, confirming that the self-assembled micelles are stable under physiological conditions. In turn, the drug release profile at pH 5.5 reveals that 44 and 48% of PTX were released in a sustained manner from PTX@AB and PTX@ABC micelles, respectively, within 48 h. These results clearly demonstrate that the release rates of PTX from PTX-loaded micelles are accelerated at the acidic medium, presumably due to the pH-induced destabilization of the micellar structures, which leads to a faster drug leakage through the micellar scaffold.

https://doi.org/10.1021/acs.biomac.1c01196
Biomacromolecules 2021, 22, 5290−5306

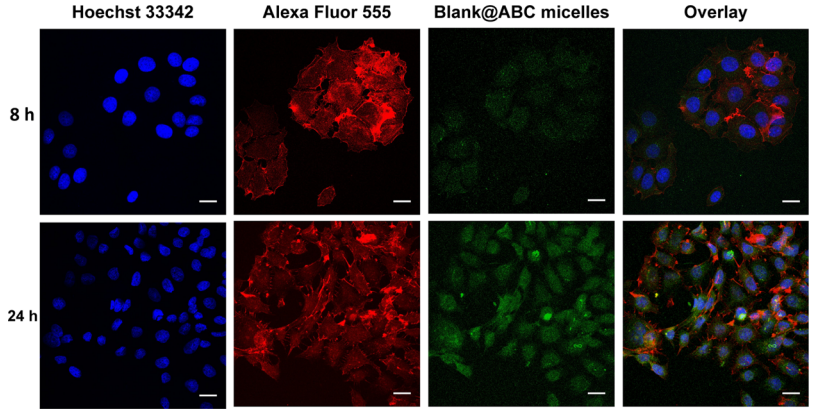

Figure 6. images of MCF-7 cells showing the subcellular localization of nuclei (Hoechst 33342-stained, blue channel), F-actin cytoskeleton (Alexa Fluor 555 phalloidin, red channel), and blank@ABC micelles (green channel). The cells were incubated with blank@ABC micelles for 8 and 24 h at 37 °C. Scale bars represent 20 μm.

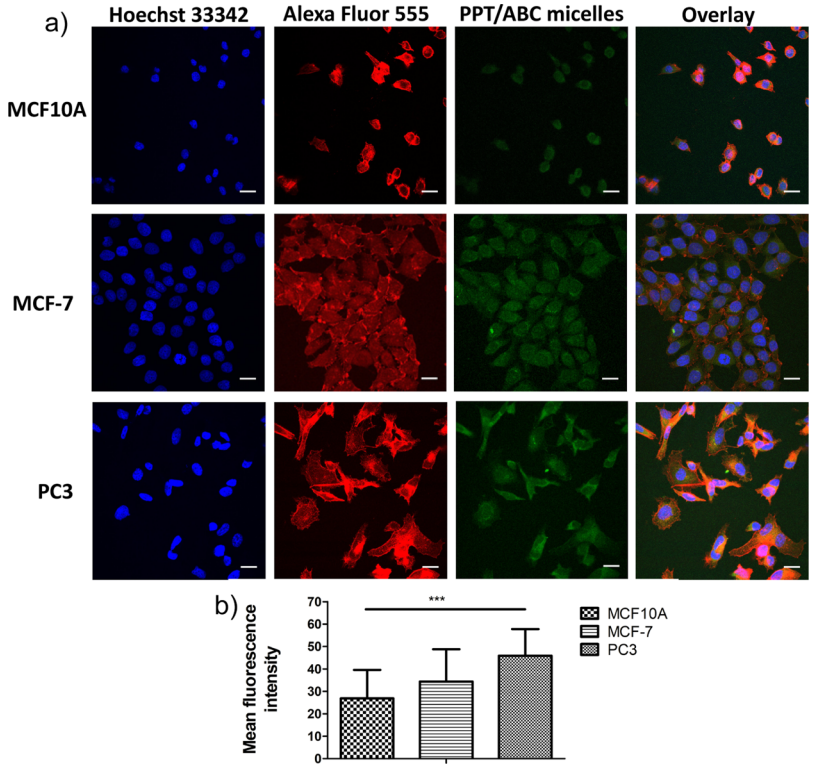

Figure 7. (a) CLSM images of MCF10A, MCF-7, and PC3 cells showing the subcellular localization of nuclei (Hoechst 33342-stained, blue channel), F-actin cytoskeleton (Alexa Fluor 555 phalloidin, red channel), and PPT/ABC micelles (green channel). The cells were incubated with PPT/ABC micelles for 24 h at 37 °C. Scale bars represent 20 μm. (b) Mean fluorescence intensity of green color between different groups (calculated using Image J software). One-way ANOVA was performed for group comparison, and significant differences were observed among all groups (***$p < 0.05$). Data are reported as mean ± SD.

From an *in vivo* point of view, the low drug release at physiological pH along with the relatively elevated and sustained release of PTX under mildly acidic conditions is a useful feature for preventing premature release into the blood stream and ensuring that the loaded drug may be effectively released inside the target tumor cells, respectively. Overall, the incomplete amount of drug released from the micelles at pH 5.5 over 48 h suggests strong hydrophobic interactions between PTX and the hydrophobic core, and stable micelles, in agreement with previous reports about micellar drugs.[86,87]

For PPT/AB and PPT/ABC micelles, a negligible amount of PPT under acidic and physiological conditions at 37 °C over 48 h was observed. In this case, we expect that an efficient release of PPT from these micelles in the tumor microenvironment occurs via enzymatic degradation upon cell internalization.

Photophysical Studies. The triblock brush copolymers present a short block containing an NIR dye designed to easily follow cellular uptake and localization of our nanosystems. The photophysical properties of monomer **Nb-dye** (**M3**), as well as the precursor cyanine dyes **6** and **7** in different organic solvents were investigated. The complete set of NIR−UV−vis absorption and emission properties for the synthesized cyanine

https://doi.org/10.1021/acs.biomac.1c01196
Biomacromolecules 2021, 22, 5290−5306

dyes is displayed in the Supporting Information (Figures S20–S33, and Table S1).

Monomer **Nb-dye** displayed an absorption band with a maximum absorption wavelength (λ_{max}) at 709–727 nm depending on the solvent (Figures S34–S40, and Table S1). Also, high molar extinction coefficients (ε) were obtained for this monomer, ranging from 5×10^4 M^{-1} cm^{-1} in THF to 14×10^4 M^{-1} cm^{-1} in DCM. Contrary to some reported cyanine dyes that are known to aggregate in solution through plane-to-plane stacking forming H-type aggregates or through head-to-tail arrangement leading to J-type aggregates,[77] our results demonstrate no tendency of monomer **Nb-dye** to form J-type aggregates and only limited amounts of H-type aggregates can be found in bands at the shorter wavelength region (hypsochromic shift) in most of the studied solvents. A similar behavior was also recently reported by us for a similar cyanine dye.[73]

The emission spectrum of monomer **Nb-dye** in the NIR region shows a maximum emission peak at around 800 nm in all solvents. As expected, monomer **Nb-dye** displayed Stokes shifts of ~90 nm that are much larger than the typical Stokes shifts of other fluorescent dyes, like its precursor *meso*-chloro cyanine dye **6** (Table S1). The large Stokes shift observed in amino-substituted cyanine dyes is frequently assigned to an intramolecular charge transfer (ICT) between the donor and the acceptor in the dyes, although clear experimental evidence of this photophysical feature has not been fully reported.[88,89] Notwithstanding, this makes it less susceptible to self-quenching and a promising candidate to be used as the fluorophore in drug delivery systems.

The NIR–UV–vis absorption and emission spectra of the cyanine dye-functionalized BBCPs in DCM and dimethyl sulfoxide displayed the same maxima locations (absorption and emission) and a band shape as the **Nb-dye**, confirming the successful introduction of the cyanine moiety into the polymers without interfering in its optical properties (Figures S41–S46, and Table S1). The absorption and emission spectra of the micelles, in 0.01 M PBS buffer at pH 7.4 (Figures S47–S49), also demonstrate the successful preservation of optical characteristics of the monomeric dye (**Nb-dye**) under aqueous conditions. Interestingly, the NIR–UV–vis absorption spectrum of blank@ABC micelles exhibited low tendency for H-aggregation in buffered aqueous solutions (Figure S47).

Cellular Uptake Assay. CLSM was employed to investigate the cellular uptake of NIR fluorescent blank@ABC and PPT/ABC micelles in tumor and normal cells. The nuclei of the cells were stained with Hoechst 33382 (presented in blue), whereas Alexa Fluor 555 Phalloidin allowed us to label the cytoskeleton (presented in red) through the binding of phalloidin to F-actin. Green color was chosen in confocal software for representing the fluorescence of the NIR dye present in blank@ABC and the PPT/ABC micelles.

As shown in Figure 6, after 8 h of incubation with blank@ABC micelles, the treated MCF-7 cell line showed some intensity of NIR fluorescence, as represented by the green color, indicating that micelles were quickly internalized into the cell membrane and diffused in both the cytoplasm and the cell nuclei. Using the same settings during the acquisition of images, it can be observed that the intensity of the fluorescent signal of blank@ABC micelles inside cells substantially increased with a prolonged incubation time (24 h).

The cellular uptake of PPT/ABC micelles was also investigated in MCF10A, MCF-7, and PC3 cells. In Figure 7a, it can be noticed that MCF-7 breast cancer cells and PC3 prostate cancer cells presented a stronger intracellular fluorescence signal than the normal breast cells MCF10A after 24 h. Indeed, the mean fluorescence intensity of green color analyzed by Image J software (Figure 7b) confirms that PPT/ABC micelles were uptaken more efficiently by cancer cells (MCF-7 and PC3) than by healthy cells (MCF10A).

To further support the cellular uptake of both blank@ABC and PPT/ABC micelles, orthogonal projections of CLSM images shown in Figures 6 and 7a were built (Figures S108–S111). The images confirm the previous findings, indicating the presence of green fluorescence from micelles inside the cell nuclei and cytoplasm.

CLSM was used only as a supporting tool to demonstrate cell uptake for this proof-of-concept study. Due to restrictions of the CLSM instrument, an excitation laser of 633 nm for the cyanine dye channel was used, and its fluorescence was detected at 661–759 nm, which are significantly far from the maxima absorption and fluorescence wavelengths in their spectra (Figures S47–S49). As a consequence, a weak fluorescence intensity of both micelles was observed, in contrast to the intense fluorescence in their emission spectra. Nevertheless, the results indicate the potential of our nanosystems as probes for biomedical imaging.

***In Vitro* Cytotoxicity Assay.** The cytotoxicity of the blank, PPT-conjugated, and PTX-loaded micelles was assessed by the colorimetric assay using the Cell Counting Kit-8 (CCK-8 assay), after incubation of cells for 48 h with varied concentrations of each compound. The *in vitro* experiments were performed using cultured monolayers of human healthy and cancer cell lines: MCF-7 (breast adenocarcinoma), PC3 (prostate adenocarcinoma), MCF10A (normal breast cells), PNT2 (normal prostate cells), and MDA-MB-231 (triple negative breast cancer cells).

Blank@AB and blank@ABC micelles displayed no significant cytotoxicity in different cell lines over the range of concentrations analyzed, with cell viabilities above 80% after 48 h treatment (Figures 8 and S89, respectively), even when the concentration of the micelles was as high as 1 mg mL^{-1}. These data are encouraging because they suggest inherent non-toxicity and good biocompatibility of the blank micelles toward a panel of different cell lines.

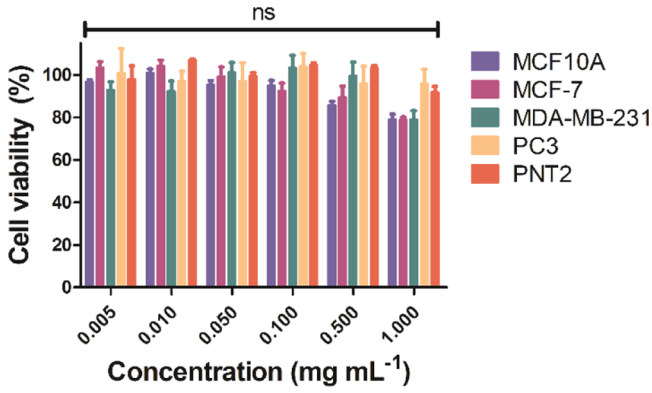

Figure 8. Cell viability of different cell lines treated with blank@ABC micelles at varying concentrations for 48 h. Data are presented as mean ± SD of two independent experiments, each one performed in triplicate. One-way ANOVA followed by Tukey's post-hoc test did not reveal a significant difference (ns) for all comparisons ($p > 0.05$).

https://doi.org/10.1021/acs.biomac.1c01196
Biomacromolecules 2021, 22, 5290–5306

PPT-conjugated and PTX-loaded micelles exhibited similar high cytotoxicity as free PPT and PTX against cancer cells (Table 3). We also used the cytotoxic 4-hydroxy-piplartine (4-HOPPT) as positive control, which after enzymatic hydrolysis should be released from the PPT-conjugated micelles. PPT/AB and PPT/ABC micelles displayed IC_{50} values of 3.0 ± 0.1 and 5.5 ± 0.7 μM, respectively, on PC3 cells, which are slightly lower than the IC_{50} value of free PPT (7.2 ± 0.4 μM).

Table 3. *In Vitro* Cytotoxic Activities of Studied Micelles and Free Anticancer Compounds against Different Human Cell Lines[a] Using the CCK-8 Assay

	IC_{50} (μM)[b]			
sample	MCF-7	MCF10A	PC3	S.I.[c]
PPT	5.3 ± 0.4	5.5 ± 0.1	7.2 ± 0.4	1.0
4-HOPPT	7.3 ± 1.1	5.6 ± 0.0	5.4 ± 0.1	0.7
AB/PPT	5.5 ± 0.2	7.9 ± 0.6	3.0 ± 0.1	1.4
ABC/PPT	6.3 ± 0.0	12.1 ± 0.8	5.5 ± 0.7	1.9
PTX	2.5 ± 0.0	3.3 ± 0.5	N.D.	1.3
PTX@AB	2.7 ± 1.3	5.2 ± 0.9	N.D.	1.9
PTX@ABC	2.6 ± 1.1	6.7 ± 0.6	N.D.	2.6

[a]MCF-7: breast cancer cell line; MCF10A: normal breast cell line; and PC3: prostate cancer cell line. [b]The half-maximum inhibitory concentration (IC_{50}) values are the mean ± SD from two independent experiments performed in triplicate per plate. [c]SI: selectivity index defined as the ratio between the IC_{50} value in the normal cell line MCF10A to the IC_{50} value in the cancer cell line MCF-7: SI = IC_{50} (MCF10A)/IC_{50} (MCF-7). ND: not determined.

No significant difference in IC_{50} values was observed for the two micelles and PPT against MCF-7 cells. These PPT-conjugated micelles were less cytotoxic than the pristine drug on normal MCF10A cells, that is, free PPT destroyed these normal cells unselectively, while treatment with the micelles could maintain higher cell viability after 48 h, as demonstrated by the higher S.I. values for the micelles. Similar outcomes were also obtained for the PTX-loaded micelles. While no significant decrease in cytotoxicity was observed for PTX@AB and PTX@ABC micelles in comparison to PTX against MCF-7 cells, micelles were more selective than the free drug against breast cancer cells. These comparative studies not only strongly suggest that micelles are effective to penetrate the cell membrane and perform controlled drug release triggered by the tumor-specific environment but also show the potential application of micelles from BBCPs as selective anticancer drug nanocarriers both via drug conjugation and encapsulation. Our nanosystems demonstrated the desirable features to minimize the side effects of two cytotoxic compounds while slightly increased the maximal therapeutic effect for targeted diseases.

CONCLUSIONS

In summary, the successful synthesis, characterization, and self-assembly of multifunctional amphiphilic poly(norbornene) BBCPs for drug delivery and biological imaging were demonstrated. Using optimized polymerization conditions and a combination of one-pot sequential grafting-through ROMP of the norbornene-based monomers, followed by halide-azide substitution and copper-free SPAAC, well-defined amphiphilic BBCPs containing hydrophilic PEG, the anticancer compound PPT, and/or a NIR fluorescent cyanine dye in their side chains were obtained. The aqueous self-assembly behavior of these amphiphilic BBCPs was investigated, which revealed spherical micelles with nanoscale sizes with the capacity to efficiently encapsulate the anticancer drug PTX. Overall, the results obtained show that our micelles are promising nanosystems for nanotheranostics and encouraging for further evaluation of *in vivo* anticancer activity in systemic delivery taking advantage of the EPR effect. Further research in our group explores the design of novel stimuli-responsive linkers, the attachment of other functionalities (e.g., targeting moieties), incorporation of degradable units within the brush copolymer backbone, and the encapsulation of other bioactive compounds, providing access to new multifunctional BBCPs with potential for nanomedicine applications.

ASSOCIATED CONTENT

Supporting Information

The Supporting Information is available free of charge at https://pubs.acs.org/doi/10.1021/acs.biomac.1c01196.

General instrumentation details; detailed experimental procedures for the synthesis of monomers, precursors, and PPT derivatives; structural characterization (^{1}H NMR, ^{13}C NMR, FT-IR, and MALDI-TOF spectra) of monomers, precursors, anticancer derivatives, and polymers; ROMP kinetic experiments; GPC traces for all the synthesized BBCPs; NIR−UV−vis absorption and fluorescence emission spectra of cyanine dye-related compounds; dose−response curves obtained in cell viability assays; and orthogonal projections of CLSM images (PDF)

AUTHOR INFORMATION

Corresponding Authors

Ronaldo A. Pilli − *Institute of Chemistry, University of Campinas (UNICAMP), Campinas, São Paulo CEP 13083-970, Brazil;* orcid.org/0000-0002-5919-7763; Email: pilli@iqm.unicamp.br

Catia Ornelas − *Institute of Chemistry, University of Campinas (UNICAMP), Campinas, São Paulo CEP 13083-970, Brazil;* orcid.org/0000-0001-8020-9776; Email: catiaornelas@catiaornelaslab.com

Marcus Weck − *Molecular Design Institute and Department of Chemistry, New York University, New York, New York 10003, United States;* orcid.org/0000-0002-6486-4268; Email: marcus.weck@nyu.edu

Author

Carolyne B. Braga − *Institute of Chemistry, University of Campinas (UNICAMP), Campinas, São Paulo CEP 13083-970, Brazil; Molecular Design Institute and Department of Chemistry, New York University, New York, New York 10003, United States;* orcid.org/0000-0003-1800-386X

Complete contact information is available at: https://pubs.acs.org/10.1021/acs.biomac.1c01196

Notes

The authors declare no competing financial interest.

ACKNOWLEDGMENTS

The authors gratefully acknowledge the Sao Paulo Research Foundation (FAPESP) (fellowships #2017/06146-8 and #2018/24020-4 for C.B.B. and research grants #2021/00555-9 for C.O. and #2019/13104-5 for R.A.P.), National Council for Scientific and Technological Development (CNPq)

(307403/2018-1 for C.O. and 307500/2015-2 for R.A.P.), and the Obesity and Comorbidities Research Center (OCRC) (2013/07607-8). This study was financed in part by the Coordination for the Improvement of Higher Education Personnel (CAPES). M.W. acknowledges financial support for this project from the National Science Foundation under award number CHE-1902917. The authors thank Dr. Douglas Soares da Silva and INCT/Inomat (FAPESP #2014/50906-9 and CNPq/MCTIC #465452/2014-0) for electron microscopy support. The authors also acknowledge the National Science Foundation (CHE-0958457) for the purchase of the MALDI-ToF mass spectrometer and the NHI for the purchase of the Avance III-600 CPTCI-cryoprobe head (S10 grant, OD016343). The authors also thank for granting access to the confocal microscope and assistance provided by the National Institute of Science and Technology on Photonics Applied to Cell Biology (INFABiC) at the State University of Campinas; INFABiC is cofunded by Fundação de Amparo a Pesquisa do Estado de São Paulo (FAPESP) (08/57906-3) and Conselho Nacional de Desenvolvimento Cientifico e Tecnológico (CNPq) (573913/2008-0).

REFERENCES

(1) Chabner, B. A.; Roberts, T. G. Chemotherapy and the war on cancer. *Nat. Rev. Cancer* **2005**, *5*, 65−72.
(2) DeVita, V. T.; Chu, E. A History of Cancer Chemotherapy. *Cancer Res.* **2008**, *68*, 8643−8653.
(3) Narvekar, M.; Xue, H. Y.; Eoh, J. Y.; Wong, H. L. Nanocarrier for Poorly Water-Soluble Anticancer Drugs-Barriers of Translation and Solutions. *AAPS PharmSciTech* **2014**, *15*, 822−833.
(4) Gala, U. H.; Miller, D. A.; Williams, R. O., III. Harnessing the Therapeutic Potential of Anticancer Drugs Through Amorphous Solid Dispersions. *Biochim. Biophys. Acta, Rev. Cancer* **2020**, *1873*, 188319.
(5) Peer, D.; Karp, J. M.; Hong, S.; FaroKHzad, O. C.; Margalit, R.; Langer, R. Nanocarriers as an Emerging Platform for Cancer Therapy. *Nat. Nanotechnol.* **2007**, *2*, 751−760.
(6) Wicki, A.; Witzigmann, D.; Balasubramanian, V.; Huwyler, J. Nanomedicine in Cancer Therapy: Challenges, Opportunities, and Clinical Applications. *J. Controlled Release* **2015**, *200*, 138−157.
(7) Arranja, A. G.; Pathak, V.; Lammers, T.; Shi, Y. Tumor-Targeted Nanomedicines for Cancer Theranostics. *Pharmacol. Res.* **2017**, *115*, 87−95.
(8) Björnmalm, M.; Thurecht, K. J.; Michael, M.; Scott, A. M.; Caruso, F. Bridging Bio-Nano Science and Cancer Nanomedicine. *ACS Nano* **2017**, *11*, 9594−9613.
(9) Shi, J.; Kantoff, P. W.; Wooster, R.; Farokhzad, O. C. Cancer Nanomedicine: Progress, Challenges and Opportunities. *Nat. Rev. Cancer* **2017**, *17*, 20−37.
(10) Barenholz, Y. Doxil - The first FDA-approved nano-drug: Lessons learned. *J. Controlled Release* **2012**, *160*, 117−134.
(11) Min, Y.; Caster, J. M.; Eblan, M. J.; Wang, A. Z. Clinical Translation of Nanomedicine. *Chem. Rev.* **2015**, *115*, 11147−11190.
(12) Tran, S.; DeGiovanni, P. J.; Piel, B.; Rai, P. Cancer Nanomedicine: A Review of Recent Success in Drug Delivery. *Clin. Transl. Med.* **2017**, *6*, 44.
(13) Anselmo, A. C.; Mitragotri, S. Nanoparticles in the Clinic: An Update. *Bioeng. Transl. Med.* **2019**, *4*, No. e10143.
(14) Sun, T.; Zhang, Y. S.; Pang, B.; Hyun, D. C.; Yang, M.; Xia, Y. Engineered Nanoparticles for Drug Delivery in Cancer Therapy. *Angew. Chem., Int. Ed.* **2014**, *53*, 12320−12364.
(15) Tee, J. K.; Yip, L. X.; Tan, E. S.; Santitewagun, S.; Prasath, A.; Ke, P. C.; Ho, H. K.; Leong, D. T. Nanoparticles' Interactions with Vasculature in Diseases. *Chem. Soc. Rev.* **2019**, *48*, 5381−5407.
(16) Astruc, D.; Boisselier, E.; Ornelas, C. Dendrimers Designed for Functions: From Physical, Photophysical, and Supramolecular Properties to Applications in Sensing, Catalysis, Molecular Electronics, Photonics, and Nanomedicine. *Chem. Rev.* **2010**, *110*, 1857−1959.
(17) Kannan, R. M.; Nance, E.; Kannan, S.; Tomalia, D. A. Emerging Concepts in Dendrimer-Based Nanomedicine: From Design Principles to Clinical Applications. *J. Intern. Med.* **2014**, *276*, 579−617.
(18) Pattni, B. S.; Chupin, V. V.; Torchilin, V. P. New Developments in Liposomal Drug Delivery. *Chem. Rev.* **2015**, *115*, 10938−10966.
(19) Grimaldi, N.; Andrade, F.; Segovia, N.; Ferrer-Tasies, L.; Sala, S.; Veciana, J.; Ventosa, N. Lipid-Based Nanovesicles for Nanomedicine. *Chem. Soc. Rev.* **2016**, *45*, 6520−6545.
(20) Ornelas, C. Brief Timelapse on Dendrimer Chemistry: Advances, Limitations, and Expectations. *Macromol. Chem. Phys.* **2016**, *217*, 149−174.
(21) Chen, G.; Roy, I.; Yang, C.; Prasad, P. N. Nanochemistry and Nanomedicine for Nanoparticle-based Diagnostics and Therapy. *Chem. Rev.* **2016**, *116*, 2826−2885.
(22) Pick, H.; Alves, A. C.; Vogel, H. Single-Vesicle Assays Using Liposomes and Cell-Derived Vesicles: From Modeling Complex Membrane Processes to Synthetic Biology and Biomedical Applications. *Chem. Rev.* **2018**, *118*, 8598−8654.
(23) Ornelas-Megiatto, C.; Becher, T.; Megiatto, J. Interlocked Systems in Nanomedicine. *Curr. Top. Med. Chem.* **2015**, *15*, 1236−1256.
(24) Owen, S. C.; Chan, D. P. Y.; Shoichet, M. S. Polymeric Micelle Stability. *Nano Today* **2012**, *7*, 53−65.
(25) Ghezzi, M.; Pescina, S.; Padula, C.; Santi, P.; Del Favero, E.; Cantù, L.; Nicoli, S. Polymeric Micelles in Drug Delivery: An Insight of the Techniques for Their Characterization and Assessment in Biorelevant Conditions. *J. Controlled Release* **2021**, *332*, 312−336.
(26) Pepić, I.; Lovric, J.; Filipovic-Grcic, J. How Do Polymeric Micelles Cross Epithelial Barriers? *Eur. J. Pharm. Sci.* **2013**, *50*, 42−55.
(27) Barnes, J. C.; Bruno, P. M.; Nguyen, H. V.-T.; Liao, L.; Liu, J.; Hemann, M. T.; Johnson, J. A. Using an RNAi Signature Assay To Guide the Design of Three-Drug-Conjugated Nanoparticles with Validated Mechanisms, *In Vivo* Efficacy, and Low Toxicity. *J. Am. Chem. Soc.* **2016**, *138*, 12494−12501.
(28) Cabral, H.; Miyata, K.; Osada, K.; Kataoka, K. Block Copolymer Micelles in Nanomedicine Applications. *Chem. Rev.* **2018**, *118*, 6844−6892.
(29) Varlas, S.; Lawrenson, S. B.; Arkinstall, L. A.; O'Reilly, R. K.; Foster, J. C. Self-Assembled Nanostructures from Amphiphilic Block Copolymers Prepared via Ring-Opening Metathesis Polymerization (ROMP). *Prog. Polym. Sci.* **2020**, *107*, 101278.
(30) Dag, A.; Cakilkaya, E.; Omurtag Ozgen, P. S.; Atasoy, S.; Yigit Erdem, G.; Cetin, B.; Çavuş Kokuroğlu, A.; Gürek, A. G. Phthalocyanine-Conjugated Glyconanoparticles for Chemo-photodynamic Combination Therapy. *Biomacromolecules* **2021**, *22*, 1555−1567.
(31) Bielawski, C. W.; Grubbs, R. H. Living Ring-Opening Metathesis Polymerization. *Prog. Polym. Sci.* **2007**, *32*, 1−29.
(32) Xia, Y.; Kornfield, J. A.; Grubbs, R. H. Efficient Synthesis of Narrowly Dispersed Brush Polymers via Living Ring-Opening Metathesis Polymerization of Macromonomers. *Macromolecules* **2009**, *42*, 3761−3766.
(33) Nomura, K.; Abdellatif, M. M. Precise Synthesis of Polymers Containing Functional End Groups by Living Ring-Opening Metathesis Polymerization (ROMP): Efficient Tools for Synthesis of Block/Graft Copolymers. *Polymer* **2010**, *51*, 1861−1881.
(34) Verduzco, R.; Li, X.; Pesek, S. L.; Stein, G. E. Structure, Function, Self-Assembly, and Applications of Bottlebrush Copolymers. *Chem. Soc. Rev.* **2015**, *44*, 2405−2420.
(35) Pelras, T.; Mahon, C. S.; Müllner, M. Synthesis and Applications of Compartmentalised Molecular Polymer Brushes. *Angew. Chem., Int. Ed.* **2018**, *57*, 6982−6994.
(36) Xie, G.; Martinez, M. R.; Olszewski, M.; Sheiko, S. S.; Matyjaszewski, K. Molecular Bottlebrushes as Novel Materials. *Biomacromolecules* **2019**, *20*, 27−54.

https://doi.org/10.1021/acs.biomac.1c01196
Biomacromolecules 2021, 22, 5290−5306

(37) Ahmed, E.; Womble, C. T.; Weck, M. Synthesis and Aqueous Self-Assembly of ABCD Bottlebrush Block Copolymers. *Macromolecules* **2020**, *53*, 9018−9025.
(38) Kuepfert, M.; Ahmed, E.; Weck, M. Self-Assembled Thermoresponsive Molecular Brushes as Nanoreactors for Asymmetric Aldol Addition in Water. *Macromolecules* **2021**, *54*, 3845−3853.
(39) Love, J. A.; Morgan, J. P.; Trnka, T. M.; Grubbs, R. H. A Practical and Highly Active Ruthenium-Based Catalyst That Effects the Cross Metathesis of Acrylonitrile. *Angew. Chem., Int. Ed.* **2002**, *41*, 4035−4037.
(40) Saha, B.; Choudhury, N.; Seal, S.; Ruidas, B.; De, P. Aromatic Nitrogen Mustard-Based Autofluorescent Amphiphilic Brush Copolymer as pH-Responsive Drug Delivery Vehicle. *Biomacromolecules* **2019**, *20*, 546−557.
(41) Shao, Y.; Jia, Y.-G.; Shi, C.; Luo, J.; Zhu, X. X. Block and Random Copolymers Bearing Cholic Acid and Oligo(ethylene glycol) Pendant Groups: Aggregation, Thermosensitivity, and Drug Loading. *Biomacromolecules* **2014**, *15*, 1837−1844.
(42) Tran, T.-H.; Nguyen, C. T.; Gonzalez-Fajardo, L.; Hargrove, D.; Song, D.; Deshmukh, P.; Mahajan, L.; Ndaya, D.; Lai, L.; Kasi, R. M.; Lu, X. Long Circulating Self-Assembled Nanoparticles from Cholesterol-Containing Brush-Like Block Copolymers for Improved Drug Delivery to Tumors. *Biomacromolecules* **2014**, *15*, 4363−4375.
(43) Zou, J.; Yu, Y.; Li, Y.; Ji, W.; Chen, C.-K.; Law, W.-C.; Prasad, P. N.; Cheng, C. Well-Defined Diblock Brush Polymer-Drug Conjugates for Sustained Delivery of Paclitaxel. *Biomater. Sci.* **2015**, *3*, 1078−1084.
(44) Johnson, J. A.; Lu, Y. Y.; Burts, A. O.; Xia, Y.; Durrell, A. C.; Tirrell, D. A.; Grubbs, R. H. Drug-Loaded, Bivalent-Bottle-Brush Polymers by Graft-Through ROMP. *Macromolecules* **2010**, *43*, 10326−10335.
(45) Patel, P. R.; Kiser, R. C.; Lu, Y. Y.; Fong, E.; Ho, W. C.; Tirrell, D. A.; Grubbs, R. H. Synthesis and Cell Adhesive Properties of Linear and Cyclic RGD Functionalized Polynorbornene Thin Films. *Biomacromolecules* **2012**, *13*, 2546−2553.
(46) Sankaran, N. B.; Rys, A. Z.; Nassif, R.; Nayak, M. K.; Metera, K.; Chen, B.; Bazzi, H. S.; Sleiman, H. F. Ring-Opening Metathesis Polymers for Biodetection and Signal Amplification: Synthesis and Self-Assembly. *Macromolecules* **2010**, *43*, 5530−5537.
(47) Vohidov, F.; Milling, L. E.; Chen, Q.; Zhang, W.; Bhagchandani, S.; Nguyen, H. V.-T.; Irvine, D. J.; Johnson, J. A. ABC Triblock Bottlebrush Copolymer-Based Injectable Hydrogels: Design, Synthesis, and Application to Expanding the Therapeutic Index of Cancer Immunochemotherapy. *Chem. Sci.* **2020**, *11*, 5974−5986.
(48) Rao, N. V.; Dinda, H.; Venu, P.; Sarma, J. D.; Shunmugam, R. Smart Nanocarrier from Norbornene Based Triblock Copolymers for the Sustained Release of Multi-Cancer Drugs. *RSC Adv.* **2014**, *4*, 45625−45634.
(49) Newman, D. J.; Cragg, G. M. Natural Products as Sources of New Drugs over the Nearly Four Decades from 01/1981 to 09/2019. *J. Nat. Prod.* **2020**, *83*, 770−803.
(50) Bezerra, D. P.; Pessoa, C.; de Moraes, M. O.; Silveira, E. R.; Costa-Lotufo, L. V.; Costa-Lotufo, L. V. Overview of the Therapeutic Potential of Piplartine (Piperlongumine). *Eur. J. Pharm. Sci.* **2013**, *48*, 453−463.
(51) Tripathi, S. K.; Biswal, B. K. Piperlongumine, A Potent Anticancer Phytotherapeutic: Perspectives on Contemporary Status and Future Possibilities as an Anticancer Agent. *Pharmacol. Res.* **2020**, *156*, 104772.
(52) Piska, K.; Gunia-Krzyżak, A.; Koczurkiewicz, P.; Wójcik-Pszczoła, K.; Pękala, E. Piperlongumine (Piplartine) as a Lead Compound for Anticancer Agents - Synthesis and Properties of Analogues: A Mini-Review. *Eur. J. Med. Chem.* **2018**, *156*, 13−20.
(53) Bezerra, D. P.; Militão, G. C. G.; de Castro, F. O.; Pessoa, C.; de Moraes, M. O.; Lima, M. A. S.; Elmiro, F. J. M.; Costa-Lotufo, L. V.; Costa-Lotufo, L. V. Piplartine Induces Inhibition of Leukemia Cell Proliferation Triggering Both Apoptosis and Necrosis Pathways. *Toxicol. in Vitro* **2007**, *21*, 1−8.
(54) Barcelos, R. C.; Pastre, J. C.; Vendramini-Costa, D. B.; Caixeta, V.; Longato, G. B.; Monteiro, P. A.; de Carvalho, J. E.; Pilli, R. A. Design and Synthesis of *N*-Acylated Aza-Goniothalamin Derivatives and Evaluation of Their *In Vitro* and *In Vivo* Antitumor Activity. *ChemMedChem* **2014**, *9*, 2725−2743.
(55) Dhillon, H.; Chikara, S.; Reindl, K. M. Piperlongumine Induces Pancreatic Cancer Cell Death by Enhancing Reactive Oxygen Species and DNA Damage. *Toxicol. Rep.* **2014**, *1*, 309−318.
(56) Ginzburg, S.; Golovine, K. V.; Makhov, P. B.; Uzzo, R. G.; Kutikov, A.; Kolenko, V. M. Piperlongumine inhibits NF-κB activity and attenuates aggressive growth characteristics of prostate cancer cells. *Prostate* **2014**, *74*, 177−186.
(57) Zheng, J.; Son, D. J.; Gu, S. M.; Woo, J. R.; Ham, Y. W.; Lee, H. P.; Kim, W. J.; Jung, J. K.; Hong, J. T. Piperlongumine Inhibits Lung Tumor Growth Via Inhibition of Nuclear Factor Kappa B Signaling Pathway. *Sci. Rep.* **2016**, *6*, 26357.
(58) Liao, Y.; Niu, X.; Chen, B.; Edwards, H.; Xu, L.; Xie, C.; Lin, H.; Polin, L.; Taub, J. W.; Ge, Y.; Qin, Z. Synthesis and Antileukemic Activities of Piperlongumine and HDAC Inhibitor Hybrids against Acute Myeloid Leukemia Cells. *J. Med. Chem.* **2016**, *59*, 7974−7990.
(59) Bezerra, D. P.; Castro, F. O.; Alves, A. P. N. N.; Pessoa, C.; Moraes, M. O.; Silveira, E. R.; Lima, M. A. S.; Elmiro, F. J. M.; Costa-Lotufo, L. V. In vivo growth-inhibition of Sarcoma 180 by piplartine and piperine, two alkaloid amides from Piper. *Braz. J. Med. Biol. Res.* **2006**, *39*, 801−807.
(60) Duan, C.; Zhang, B.; Deng, C.; Cao, Y.; Zhou, F.; Wu, L.; Chen, M.; Shen, S.; Xu, G.; Zhang, S.; Duan, G.; Yan, H.; Zou, X. Piperlongumine Induces Gastric Cancer Cell Apoptosis and G2/M Cell Cycle Arrest Both *In Vitro* and *In Vivo*. *Tumour Biol.* **2016**, *37*, 10793−10804.
(61) Xiong, X.-x.; Liu, J.-m.; Qiu, X.-y.; Pan, F.; Yu, S.-b.; Chen, X.-q. Piperlongumine Induces Apoptotic and Autophagic Death of the Primary Myeloid Leukemia Cells From Patients Via Activation of ROS-p38/JNK Pathways. *Acta Pharmacol. Sin.* **2015**, *36*, 362−374.
(62) Adams, D. J.; Boskovic, Z. V.; Theriault, J. R.; Wang, A. J.; Stern, A. M.; Wagner, B. K.; Shamji, A. F.; Schreiber, S. L. Discovery of Small-Molecule Enhancers of Reactive Oxygen Species That Are Nontoxic or Cause Genotype-Selective Cell Death. *ACS Chem. Biol.* **2013**, *8*, 923−929.
(63) Adams, D. J.; Dai, M.; Pellegrino, G.; Wagner, B. K.; Stern, A. M.; Shamji, A. F.; Schreiber, S. L. Synthesis, cellular evaluation, and mechanism of action of piperlongumine analogs. *Proc. Natl. Acad. Sci. U.S.A.* **2012**, *109*, 15115−15120.
(64) Aodah, A.; Pavlik, A.; Karlage, K.; Myrdal, P. B. Preformulation Studies on Piperlongumine. *PLoS One* **2016**, *11*, No. e0151707.
(65) Choi, T.-L.; Grubbs, R. H. Controlled Living Ring-Opening-Metathesis Polymerization by a Fast-Initiating Ruthenium Catalyst. *Angew. Chem., Int. Ed.* **2003**, *42*, 1743−1746.
(66) Pollino, J. M.; Stubbs, L. P.; Weck, M. Living ROMP of exo-Norbornene Esters Possessing PdII SCS Pincer Complexes or Diaminopyridines. *Macromolecules* **2003**, *36*, 2230−2234.
(67) Spring, A. M.; Qiu, F.; Hong, J.; Bannaron, A.; Yokoyama, S. Electro-Optic Properties of a Side Chain Poly(norbornene-dicarboximide) System With an Appended Phenyl Vinylene Thiophene Chromophore. *Polymer* **2017**, *119*, 13−27.
(68) Moatsou, D.; Hansell, C. F.; O'Reilly, R. K. Precision Polymers: A Kinetic Approach for Functional Poly(norbornenes). *Chem. Sci.* **2014**, *5*, 2246−2250.
(69) Bates, C. M.; Chang, A. B.; Momčilović, N.; Jones, S. C.; Grubbs, R. H. ABA Triblock Brush Polymers: Synthesis, Self-Assembly, Conductivity, and Rheological Properties. *Macromolecules* **2015**, *48*, 4967−4973.
(70) Slugovc, C. The Ring Opening Metathesis Polymerisation Toolbox. *Macromol. Rapid Commun.* **2004**, *25*, 1283−1297.
(71) Zhang, C.; Liu, T.; Su, Y.; Luo, S.; Zhu, Y.; Tan, X.; Fan, S.; Zhang, L.; Zhou, Y.; Cheng, T.; Shi, C. A Near-Infrared Fluorescent

Heptamethine Indocyanine Dye With Preferential Tumor Accumulation for *In Vivo* Imaging. *Biomaterials* **2010**, *31*, 6612−6617.
(72) Zhang, E.; Luo, S.; Tan, X.; Shi, C. Mechanistic Study of IR-780 Dye as a Potential Tumor Targeting and Drug Delivery Agent. *Biomaterials* **2014**, *35*, 771−778.
(73) Braga, C. B.; Perli, G.; Becher, T. B.; Ornelas, C. Biodegradable and pH-Responsive Acetalated Dextran (Ac-Dex) Nanoparticles for NIR Imaging and Controlled Delivery of a Platinum-Based Prodrug into Cancer Cells. *Mol. Pharm.* **2019**, *16*, 2083−2094.
(74) Wang, Y.; Weng, J.; Lin, J.; Ye, D.; Zhang, Y. NIR Scaffold Bearing Three Handles for Biocompatible Sequential Click Installation of Multiple Functional Arms. *J. Am. Chem. Soc.* **2020**, *142*, 2787−2794.
(75) Ornelas, C.; Pennell, R.; Liebes, L. F.; Weck, M. Construction of a Well-Defined Multifunctional Dendrimer for Theranostics. *Org. Lett.* **2011**, *13*, 976−979.
(76) Choi, P. J.; Park, T. I. H.; Cooper, E.; Dragunow, M.; Denny, W. A.; Jose, J. Heptamethine Cyanine Dye Mediated Drug Delivery: Hype or Hope. *Bioconjugate Chem.* **2020**, *31*, 1724−1739.
(77) Weinstain, R.; Slanina, T.; Kand, D.; Klán, P. Visible-to-NIR-Light Activated Release: From Small Molecules to Nanomaterials. *Chem. Rev.* **2020**, *120*, 13135−13272.
(78) Strekowski, L.; Lipowska, M.; Patonay, G. Substitution Reactions of a Nucleofugal Group in Heptamethine Cyanine Dyes. Synthesis of an Isothiocyanato Derivative for Labeling of Proteins with a Near-Infrared Chromophore. *J. Org. Chem.* **1992**, *57*, 4578−4580.
(79) Grigolo, T. A.; Braga, C. B.; Ornelas, C.; Russowsky, D.; Ferreira-Silva, G. A.; Ionta, M.; Pilli, R. A. Hybrids of 4-Hydroxy Derivatives of Goniothalamin and Piplartine Bearing a Diester or a 1,2,3-Triazole Linker as Antiproliferative Agents. *Bioorg. Chem.* **2021**, *116*, 105292.
(80) Agard, N. J.; Prescher, J. A.; Bertozzi, C. R. A Strain-Promoted [3 + 2] Azide−Alkyne Cycloaddition for Covalent Modification of Biomolecules in Living Systems. *J. Am. Chem. Soc.* **2004**, *126*, 15046−15047.
(81) Sletten, E. M.; Bertozzi, C. R. Bioorthogonal Chemistry: Fishing for Selectivity in a Sea of Functionality. *Angew. Chem., Int. Ed.* **2009**, *48*, 6974−6998.
(82) Kennedy, D. C.; McKay, C. S.; Legault, M. C. B.; Danielson, D. C.; Blake, J. A.; Pegoraro, A. F.; Stolow, A.; Mester, Z.; Pezacki, J. P. Cellular Consequences of Copper Complexes Used To Catalyze Bioorthogonal Click Reactions. *J. Am. Chem. Soc.* **2011**, *133*, 17993−18001.
(83) Abel, G. R.; Calabrese, Z. A.; Ayco, J.; Hein, J. E.; Ye, T. Measuring and Suppressing the Oxidative Damage to DNA During Cu(I)-Catalyzed Azide-Alkyne Cycloaddition. *Bioconjugate Chem.* **2016**, *27*, 698−704.
(84) Dommerholt, J.; Schmidt, S.; Temming, R.; Hendriks, L. J. A.; Rutjes, F. P. J. T.; van Hest, J. C. M.; Lefeber, D. J.; Friedl, P.; van Delft, F. L. Readily Accessible Bicyclononynes for Bioorthogonal Labeling and Three-Dimensional Imaging of Living Cells. *Angew. Chem., Int. Ed.* **2010**, *49*, 9422−9425.
(85) Fenyves, R.; Schmutz, M.; Horner, I. J.; Bright, F. V.; Rzayev, J. Aqueous Self-Assembly of Giant Bottlebrush Block Copolymer Surfactants as Shape-Tunable Building Blocks. *J. Am. Chem. Soc.* **2014**, *136*, 7762−7770.
(86) Yao, Q.; Gutierrez, D. C.; Hoang, N. H.; Kim, D.; Wang, R.; Hobbs, C.; Zhu, L. Efficient Codelivery of Paclitaxel and Curcumin by Novel Bottlebrush Copolymer-Based Micelles. *Mol. Pharm.* **2017**, *14*, 2378−2389.
(87) Takano, S.; Islam, W.; Nakazawa, K.; Maeda, H.; Sakurai, K.; Fujii, S. Phosphorylcholine-Grafted Molecular Bottlebrush-Doxorubicin Conjugates: High Structural Stability, Long Circulation in Blood, and Efficient Anticancer Activity. *Biomacromolecules* **2021**, *22*, 1186−1196.
(88) Peng, X.; Song, F.; Lu, E.; Wang, Y.; Zhou, W.; Fan, J.; Gao, Y. Heptamethine Cyanine Dyes With a Large Stokes Shift and Strong Fluorescence: A Paradigm for Excited-State Intramolecular Charge Transfer. *J. Am. Chem. Soc.* **2005**, *127*, 4170−4171.
(89) Sissa, C.; Painelli, A.; Terenziani, F.; Trotta, M.; Ragni, R. About the Origin of the Large Stokes Shift in Aminoalkyl Substituted Heptamethine Cyanine Dyes. *Phys. Chem. Chem. Phys.* **2019**, *22*, 129−135.

https://doi.org/10.1021/acs.biomac.1c01196
Biomacromolecules 2021, 22, 5290−5306